https://doi.org/10.5194/egusphere-2026-2455
Preprint. Discussion started: 11 June 2026


# Thermal regime and geometry of a hanging glacier and its interaction with permafrost: the Pointes du Mourti, Swiss Alps

Ben Robson[1], James Irving[2], Florence Magnin[3], Ludovic Ravanel[3], Coline Mollaret[4], Ludovic Baron[2], André Revil[3], Jessy Richard[3,5], Jérémie Gentizon[1], Christophe Lambiel[1]

[1]Institute of Earth Surface Dynamics (IDYST), University of Lausanne, 1015 Lausanne, Switzerland
[2]Institute of Earth Sciences (ISTE), University of Lausanne, 1015 Lausanne, Switzerland
[3]Université Savoie Mont-Blanc, CNRS, Environnements, Dynamiques et Territoires de la Montagne (EDYTEM), 73376 Le Bourget-du-Lac, France
[4]Department of Geosciences, University of Fribourg, 1700 Fribourg, Switzerland
[5]Nãga Geophysics, 73000 Chambéry, France

Correspondence to: Ben Robson (ben.robson@unil.ch)

**Abstract**

Hanging glaciers are diagnostic features of high-mountain permafrost, but their response to climate forcing and links with surrounding permafrost remain poorly understood. We investigated the hanging glacier at Pointes du Mourti (3653 m a.s.l., Swiss Alps; mean annual air temperature = -4.6 °C) between 2020 and 2025, a period that covers Switzerland's four warmest years on record. Geometric changes were quantified using uncrewed aerial vehicle photogrammetry and ice-based ground-penetrating radar, while permafrost conditions were assessed using rock surface temperatures, thermal modelling (CryoGrid2), and electrical resistivity tomography. Between 2021 and 2024, the ice thinned by up to 7 ± 0.12 m (20–45 %), with peak losses in 2022 (6.8 ± 0.5 % volume loss). Accelerated melt exposed pre-existing crevasses, enabling more efficient meltwater infiltration, which advanced basal temperature maxima and minima by ~2 months. Despite this, basal temperatures in the upper glacier remain low and continue decreasing due to enhanced winter cooling associated with ice thinning. The lower glacier exhibits temperate conditions with prolonged zero-curtain periods (146–193 days), indicating significant volumes of stored meltwater. The surrounding rock wall permafrost is discontinuous and strongly controlled by topography: only the shaded north-facing slope where the glacier lies maintains negative mean annual rock surface temperature (-3.67 °C), while sun-exposed aspects reach +3.05 °C. Model results indicate active-layer thickening that has doubled since 2015. Our observations suggest a transition toward polythermal conditions driven by rapid ice thinning, meltwater infiltration, and subsequent water storage, increasing the potential for destabilisation of small Alpine hanging glaciers under current climate conditions.

https://doi.org/10.5194/egusphere-2026-2455
Preprint. Discussion started: 11 June 2026


## 1. Introduction

Hanging glaciers (HGs) and ice aprons (IAs) are diagnostic features of mountain permafrost, which together form part of the high-mountain cryosphere. HGs are a type of unbalanced avalanching glacier, so described because they conserve their mass by quasi-periodic ice avalanches (mechanical ablation) rather than melting (Pralong & Funk, 2006). If the ice-bedrock interface is cold-based (negative temperatures), glaciers are frozen to their bedrock substrate. This occurs for high-elevation HGs located entirely in accumulation zones, where snow accumulation is mostly compensated by periodic ice avalanches occurring once a critical geometric threshold is reached. Avalanche behaviour largely depends on the geometry of the ice–bedrock interface: in a "terrace" configuration, a steepening in the bedrock causes wedge fractures in a small part of the HG frontal margin, producing small and frequent ice-release volumes ($10^3$–$10^5$ m³). Large unstable slabs form in the case of "ramp" HGs, which involve a large portion of the glacier and can release very large volumes of ice ($10^5$–$10^6$ m³) (Pralong & Funk, 2006). IAs are very small (typically < 0.1 km²) ice bodies of irregular outline, lying on slopes > 40 °, regardless of whether they are thick enough to deform under their own weight. Basal sliding is largely excluded because of cold-bed conditions, explaining the stability of ice on such steep slopes (Guillet & Ravanel, 2020; Ravanel et al., 2023). Permafrost conditions at the base of both HGs and IAs are implied (Gruber, 2005), yet the relations in the high-mountain cryosphere between these ice bodies and the surrounding and underlying permafrost remain poorly explored (Ravanel et al., 2023). However, while permafrost characteristics and distribution in steep bedrock (> 70 °) have been well investigated (Haberkorn et al., 2015; Hasler et al., 2011; Magnin et al., 2015; Weber et al., 2019), intermediately-steep slopes (38–70 °), which host the vast majority of IAs (Kaushik et al., 2021), remain insufficiently characterised (Haeberli et al., 2010).

Alpine glacier mass has been reduced by 39 % between 2000 and 2023 (The GlaMBIE Team et al., 2025). In 2022 and 2023, Swiss glaciers lost about 6 % and 4 % of their total ice volume respectively, with a further 2.5 % in 2024 (SCNAT, 2024). Such losses are unprecedented in the historical record, as losses < 2 % had previously been considered extreme (SCNAT, 2022). While 2022 was the hottest year on record for Switzerland (MeteoSwiss, 2026), much of the ice wasting has been attributed to heatwave intensity (Cremona et al., 2023). HGs and IAs are also highly sensitive to climate change. For instance, around 29 % of the original area of IAs in the Mont Blanc massif (MBM) was lost between 2001 and 2019, representing a faster rate of melting than main valley and cirque glaciers (Guillet & Ravanel, 2020; Kaushik et al., 2021). This disappearance of HGs and IAs alters surface albedo and removes thermal buffering provided by snow and ice, resulting in substantial ground warming (Bender et al., 2020; Hartmeyer et al., 2020; Hartmeyer & Otto, 2024), which in turn contributes to permafrost degradation. Permafrost in the Alps has warmed by 0.4 °C at 20 m depth between 2000 and 2019 (Etzelmüller et al., 2020). Noetzli et al. (2024) report mean warming at 10 m depth of 0.36 °C during 2013–2022, and Magnin et al. (2024) observed locally stronger warming of up to 1.0 °C in ice-poor, north-facing rock walls between 2011 and 2020. Permafrost in the MBM has already disappeared up to 3300 m a.s.l. in rock walls with a southerly aspect, which may advance as high as 4300 m a.s.l. by the end of the 21st century (Magnin et al., 2017).

https://doi.org/10.5194/egusphere-2026-2455
Preprint. Discussion started: 11 June 2026


The impact of climate change on HG stability is difficult to assess (Faillettaz et al., 2011; Pralong & Funk, 2006). Steep, high-elevation HGs are particularly sensitive to thermal changes due to surface meltwater percolation and refreezing, which efficiently transport energy into underlying ice layers (Gilbert et al., 2014). Crucially, the critical failure slope angle changes when basal temperature regimes shift from cold-based to temperate (0 °C) (Faillettaz et al., 2011). Cold-based glaciers below 4000 m a.s.l. are likely to become partially temperate by the end of the century, with many Alpine glaciers already undergoing a transition from cold to polythermal basal conditions (Gilbert et al., 2015; Pralong & Funk, 2006). Water storage in crevasses can trigger rapid destabilisation, such as documented at the Altels HG collapse in 1895 (Swiss Alps) (Faillettaz et al., 2011) and at the Marmolada glacier in 2022 (Italian Alps) (Bondesan & Francese, 2023; Francese et al., 2025). Many cold-based HGs may already be in an unstable phase where precursors to ice-avalanche events appear only days before break-off, making early warning currently feasible only for a select few glaciers (Faillettaz et al., 2011; Gilbert et al., 2015). However, glacier thermal regimes are complex and dynamic: basal cooling can occur during periods of glacier recession when ice thinning occurs but mean annual air temperatures remain well-below freezing (Irvine-Fynn et al., 2011).

HG geometry and basal thermal regimes remain poorly constrained, despite their key role in glacier stability. To address these knowledge gaps, we investigated a small, steep HG at Pointes du Mourti (3564 m a.s.l., Swiss Alps) using a multidisciplinary monitoring approach over four years. The objective was two-fold: (1) characterisation of HG surface and bedrock geometries, basal thermal conditions, and permafrost distribution; and (2) characterisation of the recent evolution of the thickness and temperature of the glacier to better understand HG response to ongoing climate forcing.

## 2. Study site and climate setting

The Pointes du Mourti (PdM; Moiry valley; Valais Alps, Switzerland) are formed of two isolated summits at 3563 and 3529 m a.s.l. connected by a rock ridge (Fig. 1, 2). Geologically, the area is part of the Dent Blanche Nappe (Lambiel et al., 2016), composed of Arolla gneiss, which is a pale green schistose granite. Being sheltered from some of the prevailing westerly weather systems, the relative dryness of the climate currently maintains the equilibrium line altitude (ELA) of glaciers in the area generally higher than 3000 m a.s.l.; however, due to the high elevations, large glaciers are still present in the region (Lambiel et al., 2016). On the north face of PdM, a small HG of 0.06 km$^2$ in **"terrace"** configuration, according to Pralong & Funk (2006), extends from close to the highest peak at 3563 m a.s.l. until 3210 m (Fig. 1). The mean slope angle is 43 ° for the main HG body, easing to 38 ° before the terminus. Significant changes have occurred at PdM during the last 80 years (Fig. 2a, b). Since 1942 the HG has lost significant thickness and surface area: IAs on the steep north face have completely disappeared, and the cirque glacier below the north face has receded and disconnected from the glacier system below.

https://doi.org/10.5194/egusphere-2026-2455
Preprint. Discussion started: 11 June 2026


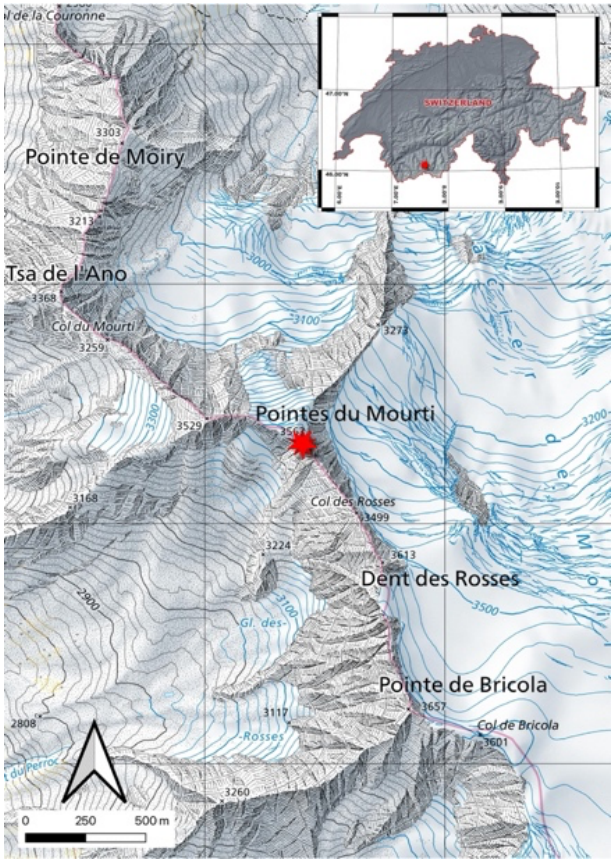


**Figure 1: Location of Pointes du Mourti with the HG on the northern flank (Base map: Swiss National Map 1:25'000, 2024 ©swisstopo)**

The presence of permafrost in the area is evidenced by significant residual massive ice exposed in a rockfall scar at the summit of the neighbouring Pointes du Bricola peak (3657 m a.s.l., 1.2 km distance; Fig. 1; Fig. S1 in the Supplementary Material). The scar formed following a large rockfall in October 2023, estimated at 40 000 m³, which lowered the summit by several metres (A. Vogel, Natural Hazards Service, Canton of Valais, personal communication, 2025).

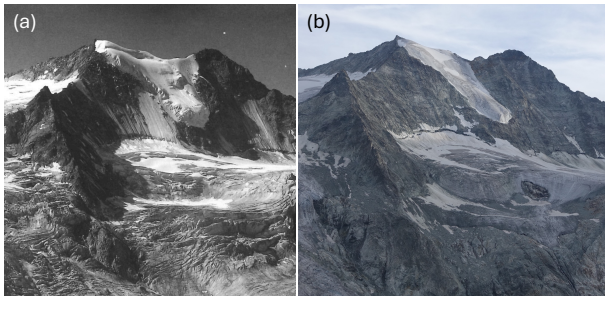


**Figure 2: View of the Pointes du Mourti (a) in 1942 (Postcard, unknown photographer), and (b) in 2020.**

https://doi.org/10.5194/egusphere-2026-2455
Preprint. Discussion started: 11 June 2026


In Switzerland, Mean Annual Air Temperature (MAAT) has risen by +3.0 ± 0.4 °C since the 1871–1900 pre-industrial reference period, which has monitored by MeteoSwiss since 1864 (MeteoSwiss, 2026). The duration of this study (August 2020 to August 2025) coincides with an exceptionally warm period relative to the 1991–2020 norm (Fig. 3). In 2022 Switzerland experienced its hottest year on record (+1.6 °C), and 2022 to 2025 were the four warmest years ever recorded (MeteoSwiss, 2026).

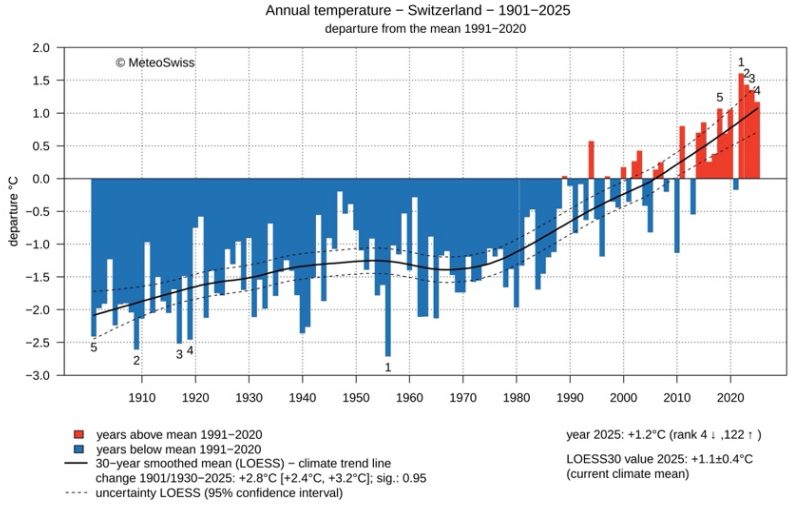


**Figure 3: Swiss annual temperature trend 1901-2025 ©MeteoSwiss**

## 3. Methods

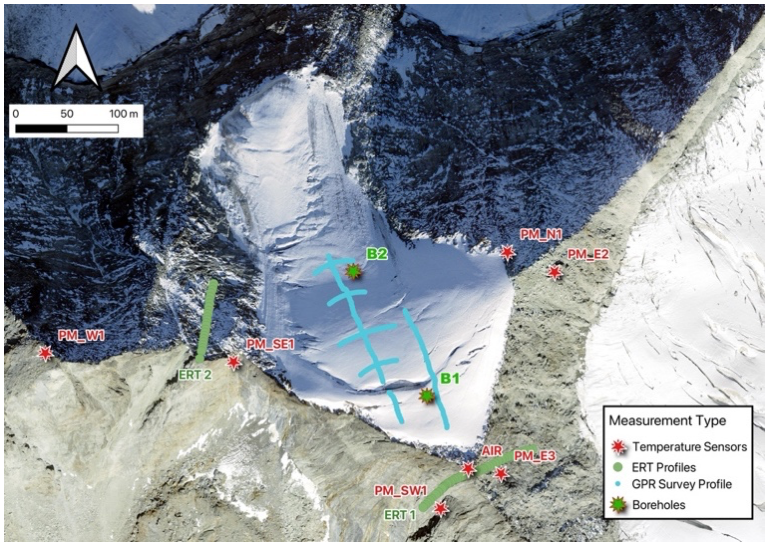


**Figure 4: Rock surface temperature and air temperature sensor locations, GPR and ERT survey profiles and location of boreholes on the PdM hanging glacier (orthophoto dated 2024, ©swisstopo).**

https://doi.org/10.5194/egusphere-2026-2455
Preprint. Discussion started: 11 June 2026


The study objectives were addressed through a multidisciplinary approach involving six principal methods (Fig. 4): (1) ground-penetrating radar (GPR) to determine subglacial bedrock geometry and ice thickness beneath the HG; (2) uncrewed aerial vehicle (UAV) photogrammetry to quantify external glacier geometry and surface change over time; (3) borehole temperature monitoring to investigate basal and englacial thermal conditions; (4) Rock-Surface Temperature (RST) measurements to characterise near-surface ground thermal regimes; (5) thermal modelling to assess permafrost evolution at depth; and (6) Electrical Resistivity Tomography (ERT) to investigate subsurface permafrost structure.

### 3.1. Ground-Penetrating Radar (GPR)

To investigate the internal geometry of the HG, we used GPR, a non-invasive geophysical technique that employs electromagnetic waves to image the subsurface and has been applied to airborne or surface based glacier studies for over half a century (Harrison, 1970; Schroeder et al., 2020). We adopted a surface-based acquisition approach to maximise measurement precision for this study. The GPR equipment is a commercially available, skid-plate mounted ImpulseRadar CrossOver 730 unit weighing 20.2 kg. It is a dual band system, providing common-offset GPR reflection data simultaneously at antenna centre frequencies of 70 and 300 MHz. The GPR is controlled by a Samsung Android tablet running the ImpulseRadar ViewPoint application (https://impulseradargpr.com/viewpoint). The tablet is worn on a chest harness, which conveniently allows hands-free operation during manoeuvres on the HG. Data were collected in continuous (time-triggered) mode. The system recorded 10 traces per second, with each trace containing 1070 samples over a time window of 1338 ns for the 70 MHz antenna, and 334 ns for the 300 MHz antenna, with $51^2$ stacks per trace to improve signal-to-noise ratio. A Topcon GR-5 dGNSS base/rover antenna pair was used in Real-Time-Kinematic (RTK) mode for precise positioning.

The GPR survey was carried out on 22.09.2022. The inclination of the survey zone ranges between 43 ° and 48 °, making it a particularly hazardous environment for data acquisition. To facilitate access and ensure team safety, we used mountaineering techniques. Static ropes were installed to descend the HG using ice screws as anchors, Abalakov threads (cord passed through two holes drilled into the ice), or combinations thereof (Fig. S2a). The descent proceeded as far as safely possible considering environmental hazards. GPR survey profiles were not pre-planned trajectories, as the optimal path needed to be determined on site. Surface conditions, such as large crevasses or areas unsuitable for building anchors, required careful consideration. We first acquired data along a down-slope profile approximately following the centre of the HG, followed by a series of shorter cross-slope profiles during the re-ascent (Fig. 4, Fig. S2b, S2c). For all profiles, the GPR antenna dipoles were oriented perpendicular to the survey direction. The corresponding data were processed in a standard workflow using customised MATLAB codes (Egli et al., 2021; Ruols et al., 2023) (Table 1).

Radar data migration was performed using a Kirchhoff algorithm, which accounts for surface topography (Allroggen et al., 2015). A radar velocity of 0.168 m $ns^{-1}$ was assumed, consistent with cold, bubble-free glacier ice (Eisen et al., 2002; Mouginot

https://doi.org/10.5194/egusphere-2026-2455
Preprint. Discussion started: 11 June 2026


et al., 2014; Murray et al., 2000). Bedrock reflections were identified in the radargrams and used to generate an interpolated, georeferenced bedrock DEM. Ice thickness was calculated as the normal distance between the UAV-derived ice-surface DEM and the bedrock DEM using a custom MATLAB workflow, producing a 0.5 m resolution thickness raster. Ice-thickness uncertainty was conservatively estimated by summing independent contributions from GPR vertical resolution (70 MHz; ± 2.15 m following Annan, 2001), manual bedrock picking (± 2 m), ice-surface interpolation (RMSE ± 0.6 m), and DEM resolution (± 0.04 m). This yields an overall uncertainty of ± 3 m per grid cell. The GPR survey covered approximately 17 000 m², from which ice volume was calculated for the surveyed area.

*Table 1: Summary of the processing steps for the dGNSS and GPR datasets*

| Step | Processing | Function |
|---|---|---|
| 1 | Data synchronisation | Use common time stamp on GPR and dGNSS datasets to determine dGNSS coordinates for every recorded trace |
| 2 | Erroneous trace removal | Traces with negligible signal strength (mean absolute amplitude < $1\times10^7$ over the first 10 samples) were removed prior to further processing |
| 3 | Data binning | Distribute GPR data into a series of 0.1 m spaced bins along the survey line of best fit direction |
| 4 | Mean trace removal | Subtract mean trace over the first 30 ns of data to remove emitted GPR pulse |
| 5 | Amplitude gain | Apply a time dependent gain function based on the average signal amplitude decay to compensate for energy spreading and attenuation |
| 6 | Migration | Apply topographic Kirchoff migration (Allroggen et al., 2015) to image the data in depth |
| 7 | Bed surface picking | Manually pick position of ice/bedrock interface |

### 3.2. Uncrewed Aerial Vehicle (UAV) photogrammetric surveys and DEM comparisons

We employed repeated UAV photogrammetric surveys to investigate the external HG geometry and surface changes over time. Quadcopter UAVs are widely used in geomorphological applications to produce high resolution digital elevation models (DEMs) and orthomosaics using Structure-from-Motion (SfM) photogrammetry (*e.g.,* Vivero & Lambiel, 2019). We used a DJI Phantom 4 RTK drone, equipped with a high precision multi frequency GNSS receiver, enabling direct georeferencing with a manufacturer stated accuracy of 0.015 m (vertical) and 0.010 m (horizontal). Given the positioning accuracies we observed (< 0.04 m), RTK constrained camera positions ensured reliable DEM generation, allowing us to omit ground control points (GCPs) from our survey design. Several studies show minimal impact on DEM precision using this approach (e.g. Stott et al., 2020; Žabota & Kobal, 2021). Doing so, we significantly reduced time requirements and minimised exposure to risk which would be encountered if equipping the field site with GCPs. Missions were planned in the DJI GS RTK application using terrain following mode and the SwissAlti3D LiDAR derived DEM in 2 m resolution from swisstopo, flying horizontal

https://doi.org/10.5194/egusphere-2026-2455
Preprint. Discussion started: 11 June 2026


transects with 70 % longitudinal and 80 % latitudinal overlaps (*e.g.*, Vivero et al., 2022), with a mix of oblique (60 °) and nadir (90 °) camera angles to improve camera calibration and reduce error (Dai et al., 2023; Kyriou et al., 2021). The dates of the 4 UAV campaigns were: 01.10.2021, 09.09.2022, 20.09.2023 and 06.09.2024.

To ensure reliable SfM-MVS processing, we followed established workflows in Agisoft Metashape Professional (James et al., 2017, 2020), except for the 2021 dataset, processed in Pix4DMapper. Inter-DEM comparisons applied standard error propagation methods (Brasington et al., 2003; James et al., 2020; Lane et al., 2003). Systematic error was checked in QGIS at 66 stable, snow free points using the Standard Deviation of Error (SDE) and Mean Error (ME) on the DEMs of Difference (DoD). SDE was below DEM resolution in all cases, indicating negligible tilting or doming. Random Error (RE) was taken as σ = DEM resolution. The limit of detection threshold between DEMs ($LoD_{95\%}$) was calculated as in Equation 1, yielding ± 12 cm for our DEMs which had 2.3–5 cm resolution.

$$LoD_{95\%} = 1.96\sqrt{\sigma_1^2 + \sigma_2^2}$$

However, the survey on 01.10.2021 was made on a cloudy day with fresh snow, and the SfM-MVS processing interpolated some surfaces on the HG, which potentially generates some errors for this DEM on the HG. Ice surface changes were evaluated by using a custom MATLAB surface-to-surface code, which measures the normal distance between the old and new surface on a 0.5 m grid resolution. Errors are propagated into the calculation using the LoD. Temporal changes in glacier thickness in the GPR survey zone were determined using the same workflow by processing the difference between the four ice surface DEMs and the subglacial bedrock DEM from the GPR survey. Uncertainty in the ice thickness in 2021 was estimated by conservatively summing independent contributions from GPR resolution (70 MHz, ± 2.15 m), manual bedrock picking errors (± 2 m), ice-surface interpolation (RMSE ± 0.6 m), and ice-surface DEM resolution (± 0.05 m), resulting in an uncertainty of ± 3 m at each grid cell, which was propagated into ice volume calculations.

### 3.3. Thermal monitoring of the glacier in boreholes

Englacial and basal temperatures were investigated within two boreholes drilled normal to the HG surface on 29.07.2021 with a Heucke steam drill (Heucke, 1999). The boreholes were equipped with GeoPrecision thermistor chains measuring temperatures hourly at 7 sensors spaced at either 2.5 m or 5 m. Data were collected annually between 29.07.2021 and 18.08.2025. Borehole B1 (3516 m a.s.l.) was drilled down to the bedrock at 12.3 m depth, with sensors positioned at 4.8 m, 7.3 m, 9.8 m and 12.3 m. By 19.08.2025, these sensor depths had transformed to 0 m (melted out), 2.0 m, 4.5 m and 7.0 m respectively due to ice ablation. Borehole B2 (3388 m a.s.l.) was drilled to 13.2 m depth, where a cavity was reached that was interpreted either as a space between the glacier and the bedrock, or a crevasse – but the bedrock was not reached. The cavity

https://doi.org/10.5194/egusphere-2026-2455
Preprint. Discussion started: 11 June 2026


was confirmed as a crevasse following the 2022 GPR survey. Sensors were positioned at 5 m, 10 m, and 5 additional sensors 'intra-cavity'. By 18.08.2025 these englacial positions had transformed to 0 m (melted out), 4.3 m, and 'intra-cavity'.

### 3.4. Rock surface temperature (RST) time series

Six GeoPrecision M-Log5W-Rock RST sensors recording temperature at 2 hour intervals were installed in August and September 2020 (RST sensor installation positions; Fig. S3). The manufacturer states an accuracy of ± 0.1 °C at 0 °C, and ± 0.3 °C from -20 to +30 °C, at a resolution of 0.01 °C. By placing sensors into drilled holes at a depth of 10 cm, the effects of direct solar radiation can be avoided, providing an effective measure of rock temperature (*e.g.*, Cathala et al., 2024; Draebing et al., 2017; Gruber et al., 2004; Haberkorn et al., 2017; Magnin et al., 2015; Rico et al., 2021). Two sensors were lost, probably due to rockfall, and were replaced in September 2023. Data are available from 5 sensors in a range of aspects (Fig. 4): PM_N1 (data: 25.09.2020–18.08.2025), PM_E2, PM_E3, and PM_SW1 (28.08.2020–18.08.2025), and PM_SE1 (20.09.2023–18.08.2025). Data from PM_W1 could not be collected due to the degraded and dangerous condition of the ridge between the two PdM summits. Air temperature (data: 30.07.2021–18.08.2025) was recorded at the higher PdM summit with a GeoPrecision M-Log5W sensor.

### 3.5. Thermal modelling

We model temperatures at depth with the CryoGrid2 model (Westermann et al., 2013), a one-dimensional transient thermal model accounting for heat conduction and latent heat exchange. The model is forced by RST daily time series and snow depth (see workflow described in Rico et al., 2021). We retained data from sensors which were not subject to significant snow accumulation so that snow depth could be assumed = 0 m at modelled points for modelling simplicity. Our criterion for this selection was the absence of long "zero-curtain" effects in spring during which snow melt maintains the temperature at 0 °C. Selected sensors were PM_N1, PM_E2, PM_E3, and PM_SW1 which lie in the N, E and SW aspects of the site. PM_SE1 was omitted from the modelling process due to winter snow cover.

We applied a standard value for the thermal conductivity of gneiss = 2.6 $Wm^{-1}K^{-1}$ (Côté & Konrad, 2005). The importance of geothermal heat flow (GHF) on ground temperature is dependent on the topographical configuration. Permafrost boundaries within rounded and wide geometries are most influenced by GHF, whereas within sharp Alpine peaks permafrost boundaries are primarily controlled by lateral heat fluxes (Magnin et al., 2017; Noetzli et al., 2007). We calculated this heat flux (Q) with the temperature offset using the Mean Annual Rock Surface Temperature (MARST) over 3 hydrological years (01.10.2021 to 31.09.2024). MARST values were then divided by the thickness of the ridge, measured in the GIS software QGIS yielding: $Q_{PM\_N1}$ = +0.071 W $m^{-2}$ (heat flux from the opposing E ridge), $Q_{PM\_E2}$ = -0.076 W $m^{-2}$ (heat flux towards the opposing N ridge), $Q_{PM\_E3}$ = -0.032 W $m^{-2}$ (heat flux towards the opposing W ridge), and $Q_{PM\_SW1}$ = +0.042 W $m^{-2}$.

https://doi.org/10.5194/egusphere-2026-2455
Preprint. Discussion started: 11 June 2026


Ground porosity values in the model describe the fraction of the volume which can be occupied by water or ice and must consider the porosity of the rock itself and the degree of bedrock fracturing. This can strongly influence the model output, because the energetic state of the ground is highly dependent on whether ground water is in a liquid or solid state due to the latent heat capacity of ice, and should therefore be accounted for (Noetzli et al., 2007; Westermann et al., 2013). We optimised the model by running: (1) a 20-year model spin up time, and (2) sensitivity tests on the porosity values. A linear model (LM) was made for each RST time series and measured air temperature from the Grand-Saint-Bernard weather station (2472 m a.s.l., 45.869167° N, 7.170556° E, situated 39 km SW from PdM; data available from https://www.meteoswiss.admin.ch/services-and-publications/service/open-data.html). Synthetic data were then generated for the RST sensors from 01.01.1934 until the start date of onsite RST measurements. Each LM was evaluated with a $R^2$ value, which were: Air = 0.95, PM_E2 = 0.77, PM_N1 = 0.71, PM_E3 = 0.80 and PM_SW1 = 0.78. Following multiple sensitivity tests on porosity values, we found no significant changes to model outputs. We therefore estimated the porosities based on our knowledge of the site characteristics: PM_N1 is in a zone of highly fractured bedrock with loose debris cover, whereas PM_E2 is in bouldery terrain, made up of variably sized loose blocks. For both these sensors we chose porosity values for the upper 5 m as 10 %. We then used assumed values of 5 % for depths between 5–10 m, and 3 % for 10–40 m depth. PM_E3 is in a zone of a both compact and fractured bedrock, with a thinner debris cover compared to PM_E2 and PM_N1. Parameters chosen were 5 % in the upper 5 m, 3 % for 5–10 m and 2 % for 10–40 m. At PM_SW1 the bedrock is compact and smooth with few fractures and no rock debris on the surface, so we selected lower porosity values of 0–5 m = 3 %, 5–10 m = 2 %, 10–40 = 2 %. Model outputs for 1934–1954 were treated as model spin up and not considered; we retained outputs between 1954 and 2025 for our analysis.

### 3.6. Electrical Resistivity Tomography (ERT)

#### 3.6.1. Field measurements

We used ERT to investigate permafrost conditions in the subsurface at PdM. ERT is a geophysical technique that estimates the spatial distribution of subsurface electrical resistivity from potential measurements corresponding to an applied electric current and is routinely used to infer permafrost extent and characteristics (Cathala et al., 2024; Duvillard et al., 2024; Hauck & Hilbich, 2024; Herring et al., 2023; Mollaret et al., 2019). We performed two ERT surveys during 19–20.08.2021 to investigate the extent of permafrost in the major slope orientations of the study site (Fig. 4), following established protocols for this method (see Herring et al., 2023; Krautblatter & Hauck, 2007; Magnin et al., 2015; Offer et al., 2025). Mountaineering techniques were required to survey the profiles on these steep rock walls. Steel electrodes were installed by drilling into the rock face. To improve electrical contact, we coated the electrodes in a wet bentonite and saltwater paste. ERT-1 covers the NE and SW faces of the south ridge extending from the summit with a 240 m long profile at 5 m electrode spacing. ERT-2 is a 120 m long profile on the north face, also at 5 m spacing (ERT profile positions, Fig. S4–S7). The position of each electrode was measured during the acquisition with dGNSS for accurate terrain reproduction in the tomograms. We used a Syscal Pro

https://doi.org/10.5194/egusphere-2026-2455
Preprint. Discussion started: 11 June 2026


from IRIS Instruments for the ERT acquisition, in the Wenner-α quadrupole configuration. The inversions of the potential measurements were carried out using the library pyGIMLi (Rücker et al., 2017). The filtering procedure (based on Mollaret et al. 2019) filtered out only 7 quadrupoles out of 360 of the ERT-1 survey, while no quadrupoles were filtered out from the ERT-2 survey, proving a high data quality. In both cases, the inversions stopped after 5 or 6 iterations when the abort criteria were reached (to avoid unnecessary iterations, either when the model fits the data within the given data error or when the change of the model between two iterations is lower than 2 %). The misfit between the generated models and the measured data is given as root-mean-square error for each ERT profile in the respective figure.

### 3.6.2. Laboratory analysis

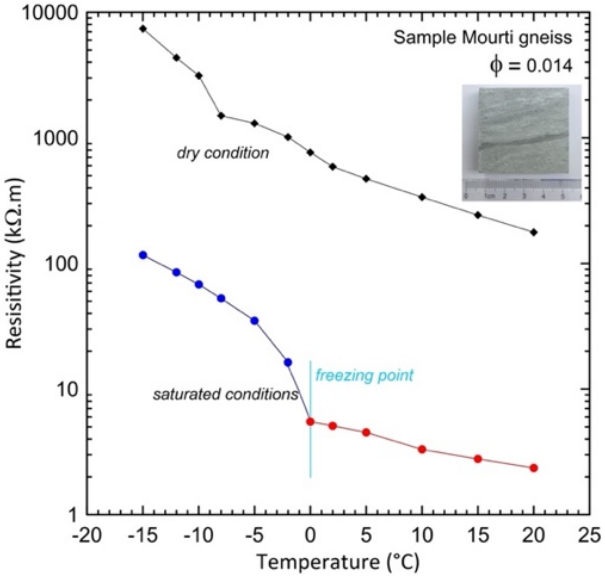


**Figure 5: Laboratory analysis of the resistivity of the Pointes du Mourti rock samples under dry (upper line) and saturated conditons (lower line).**

We performed laboratory measurements on rock samples collected in the field to study the resistivity change associated with the presence of ice, following the method developed by Duvillard et al., (2018) (Fig. 5). A rock block was first cut into 2 cubic core samples 5 x 5 x 5 cm in size, then dried for 24 h at 58 °C. One of the samples was saturated with vacuum-degassed melted snow water, while the other was left dry. The saturated sample was left for 1 month in its aqueous solution to reach chemical equilibrium before performing measurements. The other sample was kept dried and put under vacuum before measurements. We used a high precision impedance analyser ZEL-SIP04-V02 (Zimmermann et al., 2008) to perform the resistivity measurements on the saturated and the dried samples over a temperature range from –15 to +20 °C. The samples were

https://doi.org/10.5194/egusphere-2026-2455
Preprint. Discussion started: 11 June 2026


characterised by a porosity of $\phi = 0.014 \pm 0.002$ (this value is obtained from the rock sample volume, the weight difference between dry and saturated samples, and verified with 3 other rock core samples taken from the same block. The saturated sample from the summit of PdM had a resistivity of 5–35 kΩ·m between 0 and -5 °C with a strong increase in resistivity below freezing. In contrast, the dry sample remained highly resistive in the same temperature range (800–1200 kΩ·m). While these values aid interpretation of the field ERT data, resistivities measured on saturated rock samples may not be fully representative of field conditions, where rock is partly unsaturated and fractured, therefore we use these two samples as the extreme ends of the resistivity distribution when evaluating the field data.

## 4. Results

### 4.1. Hanging glacier geometry and thermal regime

#### 4.1.1. GPR campaign

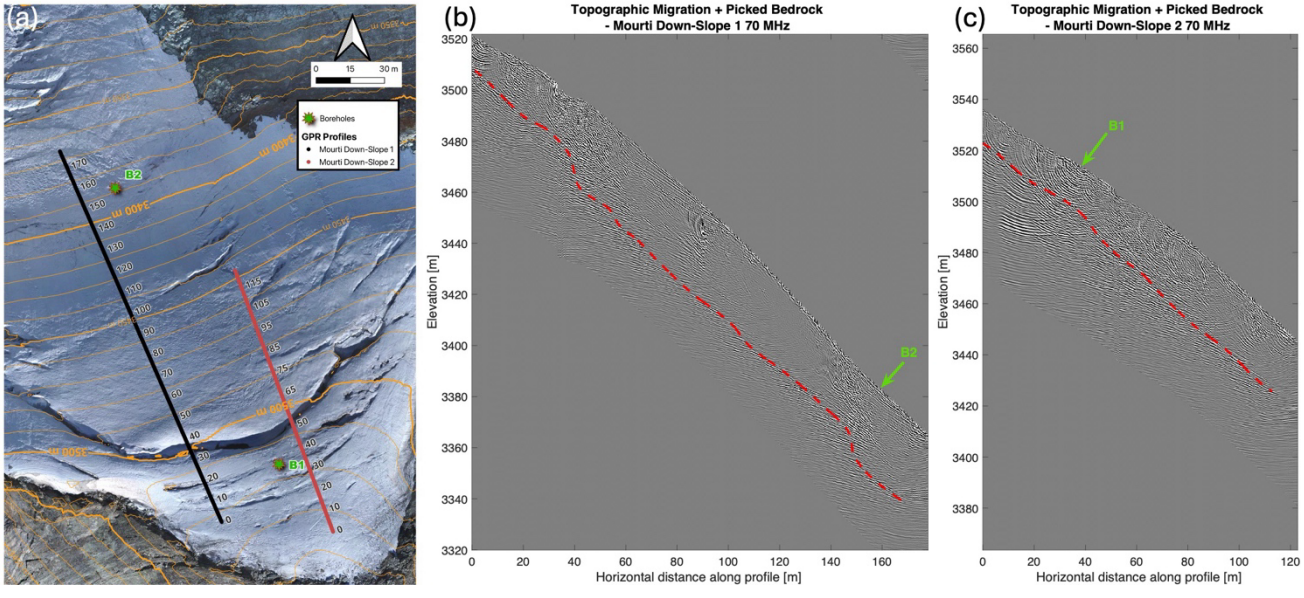


**Figure 6: The two down-slope GPR profiles on the PdM HG. (a) Position of the binned-data GPR line on the orthophoto from the UAV survey on 09.09.2022. Numbering denotes the horizontal distance travelled down profile, which corresponds with the x axis of the GPR radargrams. (b) Down-Slope 1, showing approximate location of borehole B2. The bergschrund is clearly visible at 30–40 m and another major crevasse at 140–150 m, both associated with a bedrock steepening. (c) Down-Slope-2 showing approximate location of borehole B1. Bedrock is clearly identifiable in both radargrams.**

https://doi.org/10.5194/egusphere-2026-2455
Preprint. Discussion started: 11 June 2026


The GPR campaign resulted in two down-slope profiles (Down-Slope-1 and Down-Slope-2) and four shorter cross-slope profiles (H-1 to H-4) (Fig. 4). By cross-referencing the orthomosaic dated 09.09.2022 (Fig. 6a), we can investigate several crevasses detected in the GPR data acquired on 22.09.2022. Profile Down-Slope-1 is a ~175 m long profile (Fig. 6b), which crosses the major bergschrund between 30-40 m, which results in substantial signal ringing. The wide crevasse walls were near vertical (photo, Fig. S2d). A second vertically orientated crevasse feature is crossed ~94 m on the radargram, but the orthomosaic is less clear as the surface was not open and probably represents a closed cavity in the HG. At 145-155 m there is more significant ringing in the data, suggesting a large crevasse similar to the bergschrund, yet the ice surface is again closed. However, borehole B2 was drilled on 29.09.2021 and intersected an unexplained cavity close to the lowest cross-slope survey line (profile H-4) at 13.2 m depth (Fig. 4, Fig. 6a). The two profiles indicate depths of ~27 m, leaving little doubt regarding the local ice thickness. The slope-normal depth of the vertical crevasse wall at the Down-Slope-1/H-4 intersection (green arrow, Fig. 6b) is 13 m. We therefore concluded that the borehole intersected a crevasse wall during drilling: the crevasse was sufficiently large that the steam drill ice wand dropped into the void after penetrating the crevasse wall at 13.2 m depth. Both the crevasse wall and the bedrock surface are clearly visible in the H-4 radargram as a 'double reflection' (Fig. S8). Profile Down-Slope-1 shows a significant bedrock steepening at both the bergschrund (30–40 m), and at the lowest crevasse (145-155 m). In profile Down-Slope-2 (Fig. 6c), the bedrock steepening at the bergschrund appears more shallow but the ice is clearly thicker downstream, as observed in Down-Slope 1. A well-defined vertical crevasse appears in the radargram at 85 m, which is associated with a small crevasse on the orthoimage.

#### 4.1.2. Subglacial geometry and ice thickness

The subglacial bedrock DEM covered an area of ~17 000 m², representing 20 % of the total HG area in 2022. It revealed a predominantly concave bedrock surface, particularly in the upper part of the HG, whereas the ice surface has a comparatively flatter curvature (Fig. 7a). The subglacial topography was also rugged, resulting in substantial spatial variability in ice thickness along the down-slope profiles (Fig. 6b, c). On 09.09.2022, ice thickness in the upper HG above the large bergschrund ranged between 10 and 15 m but ice deepened below the bergschrund to a maximum thickness of 31 m in the central zone. In the lower data acquisition zone, the ice thinned to 18–22 m before deepening again to 26–28 m towards the lowest extent of the surveyed area (Fig. 7b). These variations are associated with two major bedrock steepenings we identified in the GPR data, which step-down along the descent of the bedrock slope: the first parallel to the bergschrund, which explains its location, and a second toward the bottom of the surveyed area (Fig. 6b). When consulting historical imagery, a very large crevasse was visible here in 2006 (Fig. S9), which can also be explained by this bedrock configuration.

https://doi.org/10.5194/egusphere-2026-2455
Preprint. Discussion started: 11 June 2026


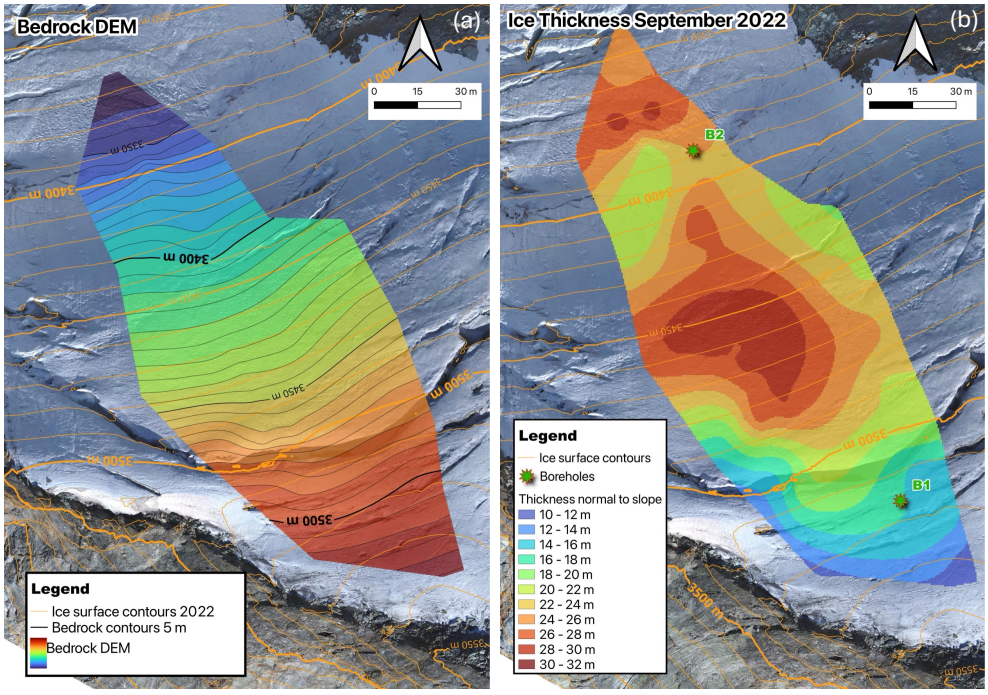


**Figure 7: Glacial geometries of the PdM HG determined by GPR and UAV surveys. (a) Sub-glacial bedrock surface contour plot, denoting a concave subglacial geometry compared to the smoother ice surface contours in orange. (b) GPR-derived ice thickness in September 2022.**

### 4.1.3. Glacier surface and volume changes

As UAV surveys were conducted in September or October of each survey year, surface changes can be evaluated over consecutive periods close to hydrological years. The largest annual surface lowering occurred during 2021–22, with a mean ice loss of 1.75 ± 0.12 m over the HG surface (Fig. 8). Due to poor UAV data quality on the lower HG surface from the 2021 survey, ice melt is underestimated, so mean melt in 2021–22 may be larger than stated. In the following years, ablation rates decreased, although surface lowering remained substantial, with mean ice losses of 0.88 m ± 0.12 m in 2022–23 and 0.83 ± 0.12 m in 2023–24. The mean surface lowering over the area available for analysis between 2021 and 2024 amounts to 2.91 m ± 0.12 m, but spatial variability in surface change is pronounced. Maximum surface lowering of up to 7.0 ± 0.12 m is observed in the less steep zones at the upper and lower extents of the HG. In contrast, the steepest central section of the glacier, located below the large bergschrund, exhibits comparatively lower ablation, generally in the range of 0.5–2.0 ± 0.12 m. This pattern is likely related to enhanced shading and reduced solar irradiation in this zone. Where ice thickness above the GPR-derived bedrock DEM is constrained (i.e., we do not calculate the volume of the full HG here), ice volume can be estimated. On 09.09.2021, the ice volume is estimated at 420 700 ± 51 430 m³. Relative volume changes over successive survey intervals

https://doi.org/10.5194/egusphere-2026-2455
Preprint. Discussion started: 11 June 2026


355 indicate a reduction of 7.4 ± 0.4 % between 01.10.2021 and 09.09.2022, 2.9 ± 0.4 % between 09.09.2022 and 20.09.2023, and 3.2 ± 0.4 % between 20.09.2023 and 06.09.2024. Cumulatively, this corresponds to a volume loss of 54 635 ± 1470 m³ over the 2021–2024 period, representing 13 ± 0.4 % of the estimated 2021 ice volume. Due to heterogeneous ice thickness and spatially variable melt rates, thickness loss was highly uneven, with maximum local thinning reaching up to 42 % of the initial thickness between 2021 and 2024.

360

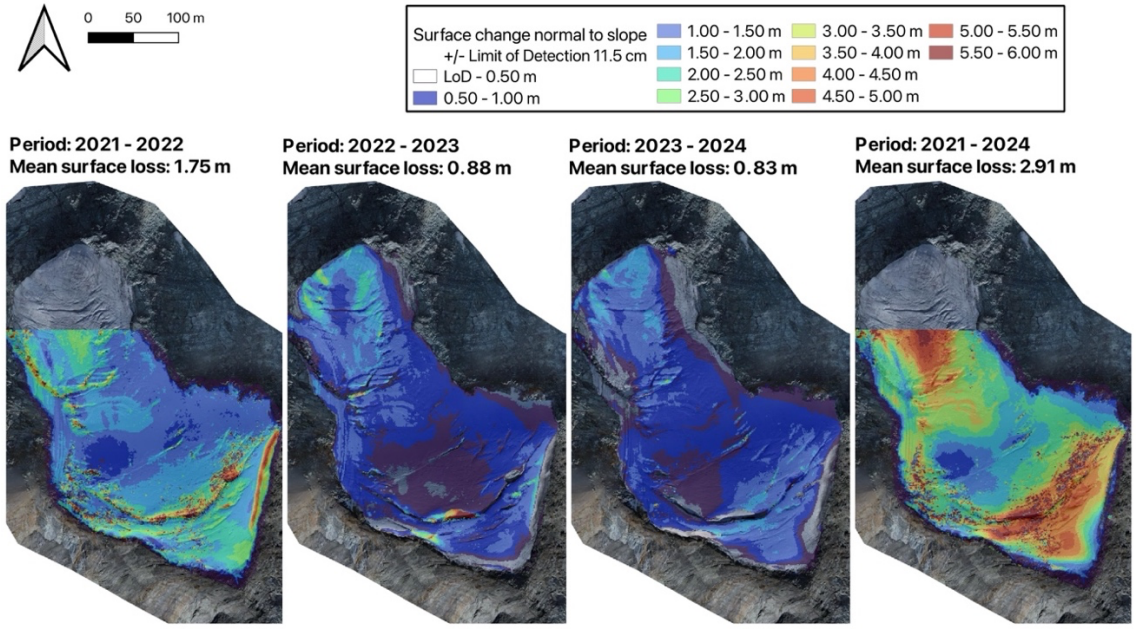


**Figure 8: Ice surface changes derived from the 4-year series of UAV flight DEMs, dating from 01.10.2021, 09.09.2022, 20.09.2023 and 06.09.2024. Derived ice thicknesses are given normal to the local slope. Missing data in the HG tongue is attributed to the smaller survey zone in 2021.**

365

### 4.1.4. Borehole temperatures

*Table 2: Ice melt values at B1 and B2 is estimated from the UAV derived DEMs for 01.10.2021, 09.09.2022 and 20.09.2023 and precisely measured from exposed thermistor cables on 06.09.2024 and 19.08.2025.*

| Ice melt by period | 29.07.2021 to 09.09.2022 | 09.09.2022 to 20.09.2023 | 20.09.2023 to 06.09.2024 | 06.09.2024 to 19.08.2025 | Total 2021 to 2025 |
|---|---|---|---|---|---|
| B1 | 3.0 m | 0.8 m | 1.4 m | 0.10 m | 5.30 m |
| B2 | 3.4 m | 0.9 m | 0.7 m | 0.70 m | 5.70 m |

https://doi.org/10.5194/egusphere-2026-2455
Preprint. Discussion started: 11 June 2026


Borehole temperatures should not be analysed without consideration of the observed ice melt at each sensor (Table 2). Total melt from 2021 to 2025 is 5.30 m at B1 (43 % of the borehole depth) and 5.70 m at B2 (~22 % of GPR-derived ice thickness), which shifted the positions of the thermistors within the glacier and caused some of them to melt out. Melt rates are highly variable, with the most significant melt occurring between 2021 and 2022, though these results are skewed by the inconsistent length of data acquisition (29.07.2021–09.09.2022 spans 13 months, 11 days).

*Table 3: Mean annual ice temperatures for hydrological years at the borehole B1 and B2, and air temperature at the summit. Thermistors are named according to their installation depth in 2021.*

| **Mean Annual Temperatures (°C) (hydrological year)** | **B1 '2.3 m'** | **B1 '4.8 m'** | **B1 '7.3 m'** | **B1 '9.8 m'** | **B1 '12.3 m'** | **B2 '5.0 m'** | **B2 '10.0 m'** | **B2 'intra-cavity'** | **Air** |
|---|---|---|---|---|---|---|---|---|---|
| 2021 – 2022 | n/a (melted) | -3.73 | -3.33 | -3.04 | -2.77 | -1.55 | -0.5 | -0.2 | -4.59 |
| 2022 – 2023 | -5.28 | -4.64 | -3.87 | -3.3 | -2.9 | -2.46 | -0.75 | -0.27 | -4.39 |
| 2023 – 2024 | -4.51 | n/a (melted) | -3.64 | -3.24 | -2.96 | n/a (melted) | -0.87 | -0.28 | -4.72 |

Mean hydrological year ice temperatures are calculated for three years (Table 3): basal temperature at B1 (B1 '12.3 m') indicates cold-based ice conditions and cools consistently between 2021 and 2024, from -2.77 to -2.96 °C. A significant cooling occurs at B2 '5.0 m', whereas mean intra-cavity temperatures remain very stable just below 0 °C. MAAT at the summit varies between -4.39 and -4.72 °C without any significant trend.

Figure 9 shows daily mean temperatures during the data acquisition period. Air temperatures ranged from -24.2 °C on 20.01.2023 to +10.5 °C on 06.09.2023. During the 2021–2022, 2022–2023, and 2023–2024 hydrological years there were 122, 122, and 108 melt days, respectively. Temperature minima propagate to progressively later dates as the winter cooling affects the glacier, while temperature amplitude decreases with depth. For example, the B1 '7.3 m' sensor reached -4.41 °C on 06.06.2022, the '9.8 m' sensor reached -3.56 °C on 06.07.2022, and the basal '12.3 m' sensor reached -3.05 °C on 12.08.2022. Maximum temperatures followed the same cascading pattern.

https://doi.org/10.5194/egusphere-2026-2455
Preprint. Discussion started: 11 June 2026


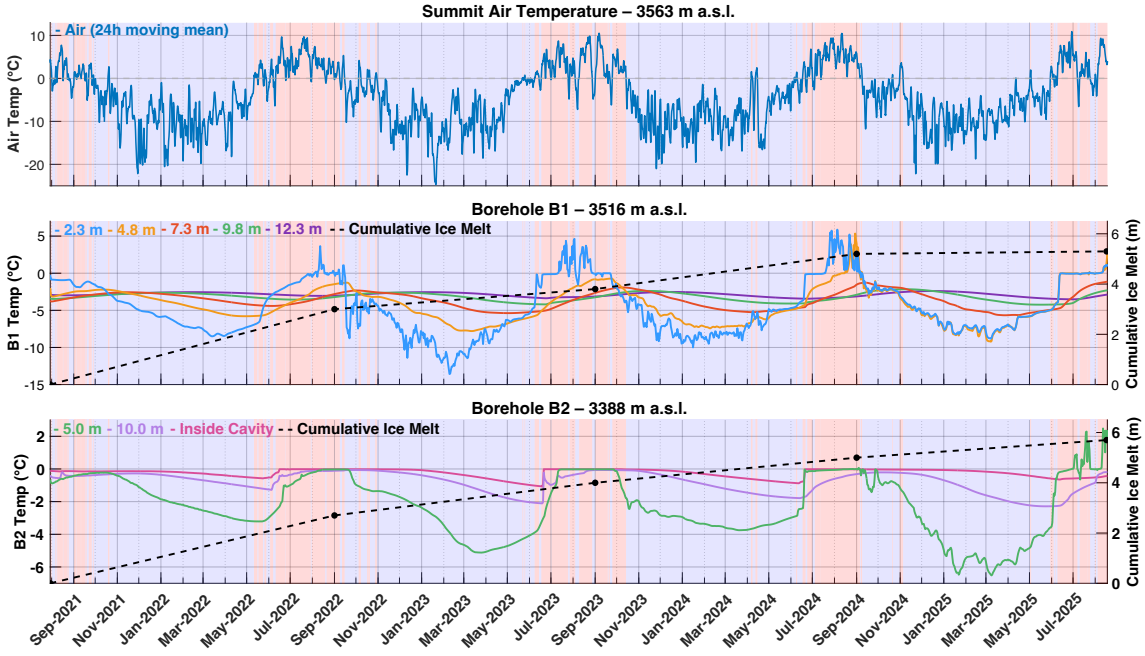


**Figure 9: Air and borehole daily mean temperatures between 04.08.2021 and 17.08.2025. (Top) Air temperature at the summit of PdM, (Middle) borehole B1. (Bottom) borehole B2. The blue background indicates periods of negative air temperatures, while the pink one indicates periods of positive air temperatures sustained for more than 24 hours, which we assume induces snow or ice melt. Cumulative ice melt measured from the ice surface DEM and thermistor cable emergence is indicated with the dashed black line.**

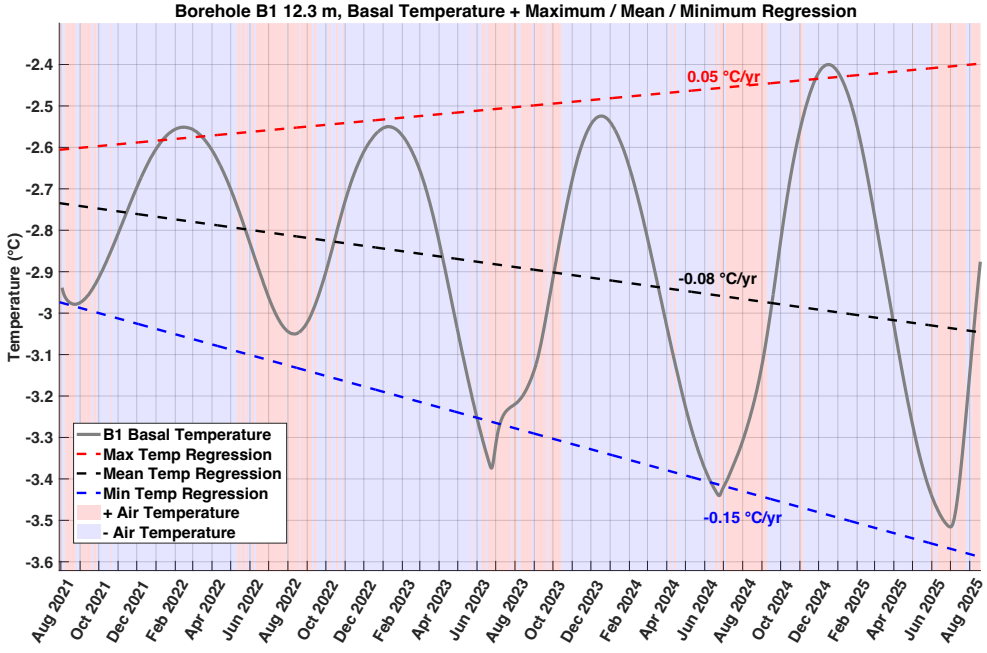


**Figure 10: Borehole B1 basal temperature between 04.08.2021 and 18.08.2025. Ice thickness reduced by 5.3 m (~43 % of total) during the same period.**

https://doi.org/10.5194/egusphere-2026-2455
Preprint. Discussion started: 11 June 2026


Borehole B2 measures englacial temperatures only, as none of the installed sensors could be placed at the ice–rock interface. The five thermistors located "intra-cavity" produced almost identical readings, therefore only one is shown here. Seasonally temperate ice locally exists within borehole B2. A strong and rapid increase in ice temperature occurs at all sensors yearly in June, coinciding with snow and ice surface melt conditions, though this response becomes more rapid from 2023 onwards. On 20.06.2023, B2 '10.0 m' increased from -2.1 °C to -0.1 °C in 8 hours, and B2 'intra-cavity' increased from -1.0 °C to 0.0 °C in 5 hours. B2 '5.0 m' responded more gradually, warming from -3.9 °C on 09.06.2023 to 0.0 °C on 12.07.2023 (following zero-curtain duration: 78 days). Similarly, in 2024, B2 '5.0 m' increased from -1.7 °C to 0.0 °C in 2 hours on 19.06.2024 (zero-curtain duration: 79 days), and the following day B2 'intra-cavity' increased from -0.7 °C to 0.0 °C in 5 hours. B2 '10.0 m' also warmed during this event but more slowly, reaching a maximum of -0.2 °C in October 2024. B2 '5.0 m' experienced a zero-curtain from 14.08.2022 to 21.09.2022 (39 days), and B2 '10.0 m' from 08.09.2022 to 30.10.2022 (53 days). B2 'intra-cavity' experienced very long zero-curtain durations: 16.06.2022–24.12.2022 (192 days), 21.06.2023–13.11.2023 (146 days), and 21.06.2024–20.12.2024 (183 days). We interpret this as an influx of a large amount of water into the cavity which is stored for long periods. These results show that a column of seasonally temperate ice extends to at least 7.4 m depth in 2022; 6.7 m in 2023 (-0.01 °C to -0.06 °C for both periods); and 5.6 m in 2024 (temperatures of -0.01 °C intra-cavity to a maximum of -0.20 °C at B2 '10 m'). In contrast, during the 2025 melt period and until the end of available data on 18.08.2025, temperatures remained further below 0 °C, suggesting that liquid water no longer pooled around the sensor and indicating a change in englacial hydrology.

Basal temperature is directly measured at B1 '12.3 m' (Fig. 10) and remains below freezing, with a minimum of -3.52 °C on 01.07.2025 and a maximum of -2.40 °C on 17.12.2024, indicating a cold-based thermal regime. Basal temperature cools overall at a rate of -0.08 °C $yr^{-1}$, in contrast to air temperature which increased slightly by +0.40 °C $yr^{-1}$ over the same period. Maximum basal temperatures remained almost stable during the first three years, with a small increase in winter 2024–25 producing a weak positive trend (+0.05 °C $yr^{-1}$). In contrast, minimum temperatures show a cooling trend (-0.15 °C $yr^{-1}$), which drives the mean cooling signal. The amplitude between maximum and minimum temperatures increases through time, and the timing of maxima and minima advances significantly. Maximum temperatures occur on 14.02.2022, 07.01.2023, 20.12.2023, and 16.12.2024, representing an advance of basal thermal maximum of almost two months between 2021 and 2025. Minimum temperatures are reached on 23.08.2021, 13.08.2022, 25.06.2023, 24.06.2024, and 01.07.2025. Data availability in 2021 is limited due to the late installation date (29.07.2021); however, in both 2021 and clearly in 2022, surface melt does not immediately trigger basal warming. From 2023 onwards, the minimum temperature event is much more closely associated with the snowmelt proxy date, whereby basal warming occurs rapidly after sustained surface melt conditions. There is a particularly abrupt response on 25.06.2023, suggesting that basal temperatures are increasingly influenced by water infiltration to the glacier base and warming is induced by latent heat release during refreezing of water.

https://doi.org/10.5194/egusphere-2026-2455
Preprint. Discussion started: 11 June 2026


## 4.2. Permafrost conditions

### 4.2.1. Rock surface temperatures (RST)

*Table 4: Mean Annual Air Temperature (MAAT) and Mean Annual Rock Surface Temperature (MARST)*

| MARST & MAAT (°C) (hydrological year) | Air | PM_E2 | PM_E3 | PM_N1 | PM_SW1 | PM_SE1 |
|---|---|---|---|---|---|---|
| 2020–2021 | n/a | 0.11 | 2.54 | -4.09 | 0.74 | n/a |
| 2021–2022 | -4.59 | 2.01 | 3.36 | -3.60 | 2.25 | n/a |
| 2022–2023 | -4.39 | 1.51 | 3.18 | -3.47 | 2.02 | n/a |
| 2023–2024 | -4.71 | 1.51 | 3.12 | -3.48 | 1.39 | 2.21 |
| **Mean Temperature** | **-4.56** | **1.29** | **3.05** | **-3.67** | **1.60** | **2.21** |

MARST and MAAT were calculated for the hydrological years (01.10 – 30.09) 2021–2024 (Table 4). $MAAT_{2021–2024}$ = -4.56 °C, indicating favourable air temperatures for permafrost at PdM. The only negative MARST was measured at PM_N1 (-3.67 °C). At the three other sensors, positive MARSTs are observed, with PM_E3 being the warmest location (3.05 °C). MARST at all locations shows a consistent warming trend during the data acquisition period (approximately 4 years, 11.5 months) of +0.19 °C $yr^{-1}$ at PM_N1, +0.25 °C $yr^{-1}$ at PM_E2, +0.17 °C $yr^{-1}$ at PM_E3, and +0.17 °C $yr^{-1}$ at PM_SW1. In contrast, MAAT is stable at +0.01 °C $yr^{-1}$ (see also: Fig. S10).

Considering the daily mean temperatures (Fig. S11), PM_E3 and PM_SW1 show undamped temperature variability, consistent with largely snow-free conditions. A short zero-curtain of between 6 – 13 days is observed at PM_N1, which indicates a short snow melt period, and winter temperatures variations are moderately damped. No zero-curtain periods occur at PM_E2, but winter temperatures are similarly damped, suggesting the presence of a thin insulating snow cover. PM_SE1 is subject to thick snow cover, with a 133 day zero-curtain in 2024 during snow melt.

https://doi.org/10.5194/egusphere-2026-2455
Preprint. Discussion started: 11 June 2026


#### 4.2.2. Thermal modelling

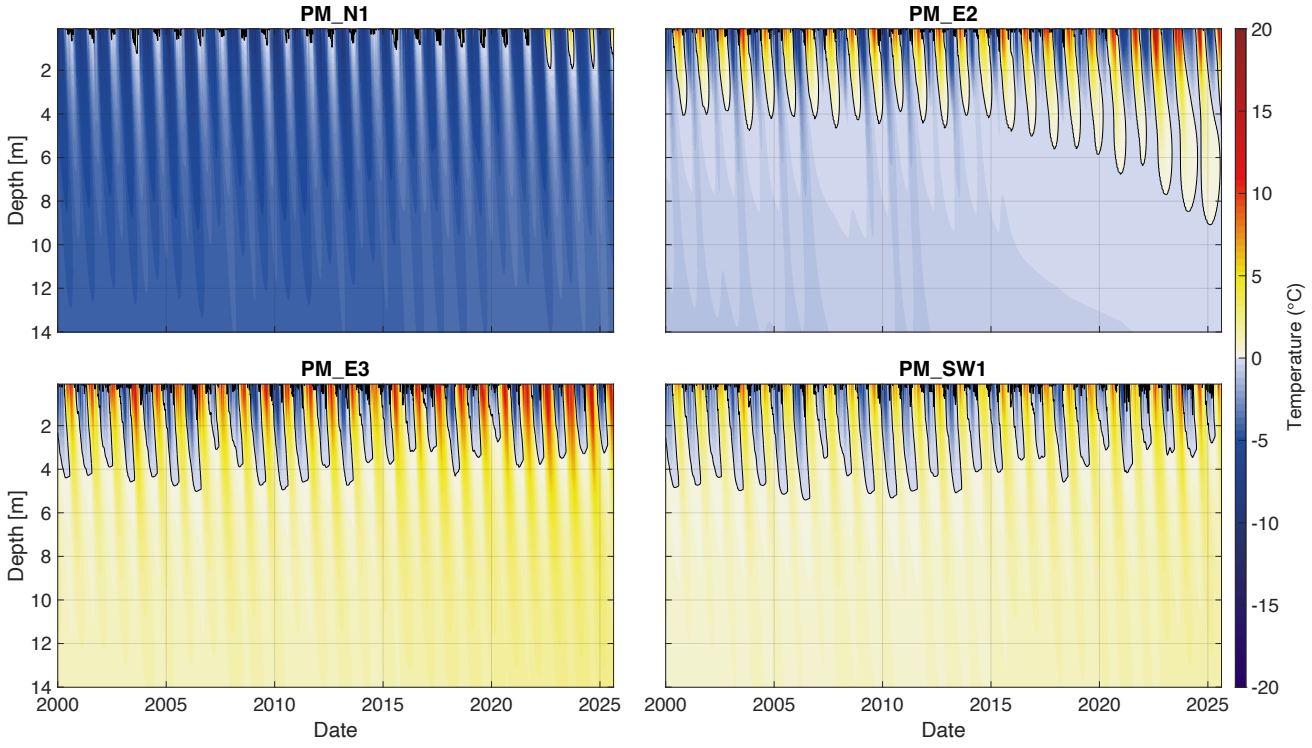


**Figure 11: Ground temperature modelling results from 2000–2025 with CryoGrid2 for RST sensors PM_N1, PM_E2, PM_E3 and PM_SW1, displayed to 14 m depth.**

Ground temperature modelling indicates the presence of permafrost at PM_N1 and PM_E2 (Fig. 11). We observe a pronounced active layer thickening driven by the strong increase in RST recorded in the data since 2021 (Table 4 and Fig. S11). PM_N1 ($MARST_{2020–2024}$ = -3.67 °C) indicates cold permafrost conditions (below -2 °C), below the active layer. Active layer thickness (ALT) remained relatively stable from 2000 to 2021, except in 2003, which was the hottest summer ever recorded in Switzerland (MeteoSwiss, 2026). ALT then more than doubled in 2022, 2023 and 2024. At PM_E2 ($MARST_{2020–2024}$ = 1.29 °C), we modelled warm permafrost conditions (-2 to 0 °C). ALT remained relatively stable from 2000 to 2014, increased from 2015 to 2024, more than doubling in depth with a linear trend throughout this 10 year period. We also observe a warming trend beginning in 2003 at 8–10 m depth. At PM_E3 ($MARST_{2020–2024}$ = 3.05 °C), and PM_SW1 ($MARST_{2020–2024}$ = 1.60 °C), the model indicates positive temperatures below roughly 10 m, meaning absence of permafrost. The sensors are opposite each other on a thin rock ridge (Fig. 4 and Fig. S4–S7) which is heated by solar irradiation, contributing to the warming at depth from two aspects. Maximum winter freezing depth was reduced by ~40 % in 2000–2025 at both locations.

https://doi.org/10.5194/egusphere-2026-2455
Preprint. Discussion started: 11 June 2026


### 4.3.3. Electrical Resistivity Tomography (ERT)

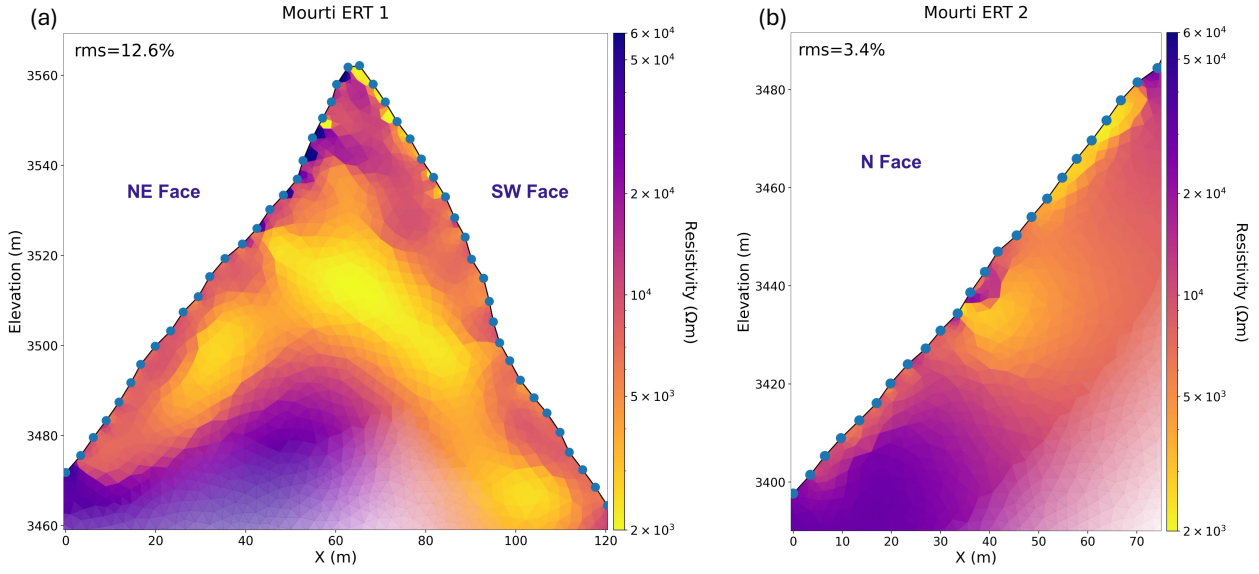


**Figure 12: ERT profiles from the 2 surveys made on 19–20.08.2021. Electrode spacing was 5 m (denoted with blue dots). See location on Figure 4. (a) Profile ERT-1, a 240 m long profile (48 electrodes) spanning the south summit ridge, viewed as looking towards the south from the summit. (b) Profile ERT-2 is a 120 m long profile (24 electrodes) on the north face on the thin west summit ridge.**

ERT-1 (Fig. 12a, Fig. S4–S7) shows surface conditions on both slopes generally highly resistive (red hues; ~7 kΩ·m), which are attributed to unsaturated weathered bedrock rather than frozen ground, as the survey was carried out in summer. A core of yellow-orange low resistivities (2–5 kΩ·m) occurs near the centre of the profile, between depths of 5–20 m on the NE side and 5–25 m on the SW side, indicating probable unfrozen ground. Given the positive ground surface conditions (MARST, PM_E3 = 3.05 °C; MARST, PM_SW1 = 1.60 °C) and thermal modelling indicating the absence of permafrost on these aspects (Fig. 11), the presence of liquid water is plausible, creating a conductive medium, regardless of whether ground ice is also present in the fracture matrix. The upper part of the ridge (3540–3562 m a.s.l.) forms a zone of high resistivities (purple, ~20 kΩ·m), indicating locally frozen conditions. The pyramidal summit geometry enhances the thermal influence of the cold north face in this small zone, suggesting this is an area of permafrost linked to the observed freezing temperatures on the north face (MAAT = -4.6 °C, MARST, PM_N1 = -3.7 °C) and the HG. At the base of the profile (3455–3490 m a.s.l.), a core of high resistivities (purple, ~30–50 kΩ·m) is modelled where the ridge is 90–120 m thick. The elevated resistivities indicate the presence of permafrost at depth where the ground is sufficiently insulated from observed warm surface conditions.

At ERT-2 (Fig. 12b), the upper ~5 m in the upper part of the profile shows low resistivities (yellow, ~2–3 kΩ·m), indicating unfrozen ground. Midway along the profile, a core of low resistivities (yellow, ~3 kΩ·m) coincides with a ledge feature on the ground surface (orthoimage: Fig. 4). This feature may trap water or act as the outlet of moisture from a fault line identified

https://doi.org/10.5194/egusphere-2026-2455
Preprint. Discussion started: 11 June 2026


above the profile producing locally higher conductivity. In the lower part of the profile, the upper ~5 m shows moderate resistivities (orange to dark orange, ~6–10 kΩ·m), attributed to the observed dry conditions (i.e. non saturated) rather than frozen ground. RST at PM_N1 in a comparable topographic setting recorded consistently positive daily mean temperatures (up to 5.9 °C) for between 27.06.2021–26.08.2021, and thermal modelling indicates that the ALT reached its maximum around this date (Fig. 11), so the ground surface was not frozen. We therefore interpret the shallow conductive zone (3400–3430 m) as the active layer. At greater depth, resistivities increase sharply to form a high resistivity core (purple, ~20–30 kΩ·m), interpreted as frozen. This occurs at much shallower depth (~8 m) than in ERT-1 (~20 m), consistent with colder conditions observed on the shaded north face. In the lower part of the profile the ridge cross-section is thicker (varies from 145 m at electrode 1; 85 m at electrode 8; 3 m at electrode 24) and thus better insulated from the warm south facing slope on the opposite side (MARST, PM_SE1 = 2.21 °C). In contrast, the thin upper ridge remains strongly influenced by lateral heat flux from the warmer south facing slope, explaining the absence of permafrost and the relatively low interior resistivities (orange, ~5–10 kΩ·m).

## 5. Discussion

### 5.1. New knowledge on HGs geometries and evolution

Subglacial bedrock geometry is concave under the PdM hanging glacier, which may explain why the HG formed in this location. Given the requirement for cold-based ice, glacial-bedrock erosion will be minimal and will thus not have significantly contributed to the development of this subglacial morphology. In contrast, the planar rock walls to the NE of the glacier hosted an ice-apron in the 1942 photograph (Fig. 2a), which had not developed into a HG, and which has since disappeared (Fig. 2b). We showed that the ice thickness is quite significant: up to 31 m determined by GPR. This is comparable to similar small, steep HGs, for example at Mallory glacier, MBM, French Alps (up to 29 m; Cailhol et al., in prep.). These are much thinner than depths reported from HGs connected into larger glacier systems (up to 103 m, Taconnaz glacier, MBM; Gilbert & Vincent, 2013). The two distinct bedrock steepenings we identified in the GPR data appear to be determining factors for the location of major crevasses, which nevertheless fill and reappear over time. A large bergschrund is currently present, but was frequently smoothed over in historical images (for example in 2006; Fig. S9). This is also case for the large lower crevasse visible in 2006. These data suggest the bedrock strongly determines crevasse locations, which manifest in vertical orientations.

The magnitude of ice loss from the surface between 2021 and 2025, with local melt rates of up to 7 m, represents the removal of 20–45 % of the 2021 ice thickness and demonstrates exceptional melt intensity. In comparison, 6.2 m of ice thinning was reported between approximately 2000 and 2020 at an ice apron between 3570–3690 m a.s.l. in the MBM (~55 km WSW of PdM; Ravanel et al., 2023). Ice volume losses are extreme (up to 7.4 ± 0.4 % between 01.10.2021 and 09.09.2022), comparable to ice volume losses observed across Swiss glaciers in 2022 (6.2 %; SCNAT, 2022). Even in years with above average spring

https://doi.org/10.5194/egusphere-2026-2455
Preprint. Discussion started: 11 June 2026


snow accumulation, exceptionally warm summers drove high melt rates. Spring 2024 was notably snowy at high elevations (up 177 % of precipitation compared to the 1991-2020 norm in Switzerland) (MeteoSwiss, 2025). Nevertheless, this snow accumulation was insufficient to prevent a mean ice thickness loss of 0.83 m by the end of the summer of 2024. This response is consistent with Cremona et al. (2023), who demonstrated that the exceptional glacier mass losses observed in 2022 were primarily driven by persistent summer heatwave conditions rather than anomalies in winter snow accumulation.

Spatial and temporal heterogeneity in ice loss is evident, with the lower angle upper and lower HG sections experiencing up to six times more melt than the steep central section. Melt rates at borehole B1 varied markedly between years (Table 2), with losses of up to 3 m in 2022, 0.8 m in 2023, 1.4 m in 2024, and only 0.10 m measured on 19.08.2025, despite 2025 being the fourth hottest year on record (MeteoSwiss, 2026). In contrast, 0.70 m of melt was measured at borehole B2 in 2025, consistent with the previous year. This spatial contrast likely reflects the intermittent development of a protective snow cover which was observed on the upper elevations of the HG and highlights the sensitivity of local melt rates to short term meteorological conditions superimposed on regional scale warming trends.

The HG terminus is exposed to sustained summer ablation. No ice avalanches were observed during the monitoring period, challenging classical concepts of unbalanced avalanching glaciers (Pralong & Funk, 2006). The potential absence of quasi periodic ice avalanche activity, combined with ~18 % ice thickness loss at the terminus between 2022 and 2024 – and logically further loss during 2025 – suggests that ice flux toward the glacier front has become critically limited. Very low glacier velocities are further indicated by repeat position measurements of B2 (3388 m a.s.l.), which show a downslope displacement of only ~5 m over five years. This measurement is complicated by the effects of surface lowering on a 45 ° slope: being above the bergschrund, displacement should be minimal at B1, yet its position displaced negatively with respect to ice flow direction by 1.55 m. Together, these observations demonstrate significant changes to the surface geometry of the HG, a functional decoupling from its climatic and dynamic equilibrium, consistent with a transition toward a transient, rapidly wasting ice body rather than a dynamically sustained avalanching glacier.

### 5.2. Thermal regime of the hanging glacier

The loss of significant ice volumes from the HG surface has resulted in the percolation of large quantities of meltwater into the HG body. Our temperature data provide multiple lines of evidence for the increasing influence of water infiltration on the internal and basal thermal regime of the HG, but the effect on ice temperature depends on the location on the HG in the case of PdM. The cooling response at B1 (–0.08 °C $yr^{-1}$; Fig. 10) is consistent with increasingly efficient winter cooling as ice thickness is reduced (Irvine-Fynn et al., 2011). Maximum basal temperatures at B1 have remained relatively stable despite substantial ice thinning, which likely reflects the buffering effect of latent heat consumption during melt, whereby incoming energy is preferentially used for phase change rather than increasing ice temperature. MAAT at the PdM summit (3563 m

https://doi.org/10.5194/egusphere-2026-2455
Preprint. Discussion started: 11 June 2026


a.s.l.) remained stable over the same period (no significant trend; Fig. S10), indicating that observed cooling at the base of the glacier is not directly coupled to atmospheric forcing. The development of efficient water pathways through crevasses and englacial channels has the potential to accelerate heat transfer to depth from infiltrated water (Gilbert et al., 2014). Although our data from 2021 is limited in range, basal temperatures continued cooling for several months after the onset of surface melt in 2021 and 2022, whereas from 2023 onward basal temperatures responded immediately to the onset of surface melt (Fig. 10). We suggest that the extensive crevasse opening observed during the exceptionally hot summer 2022 (orthomosaic; Fig. 6a) was a key control on this response transition. However, the ice is cold-based at B1 (-2.96 °C, 2023-2024) and continues to cool, which firmly suggests superior part of the HG above the bergschrund is stable.

Thermal conditions at B2 (3388 m a.s.l.) differ fundamentally from those at B1. Water accumulates at B2 in potentially large quantities given the very long zero-curtain periods (up to 193 days), with sufficient thermal inertia to maintain locally temperate ice conditions even into winter. Internal crevasse volume is likely significant, as the surface was open in the 2006 historical image (Fig. S9). At least the upper ~31 % of the B2 ice column is partially temperate (ice depth at $B2_{2022}$ = ~24 m, B2 '10m sensor depth in 2022 = 7.34 m), suggesting either a basal cold layer overlain by temperate ice or a predominantly temperate regime at this location. If the basal regime of the HG is indeed polythermal, this has important implications for its future stability and dynamic behaviour. Relevant failure mechanisms for the PdM HG are either: (1) loss of basal adhesion on the bedrock surface caused by temperate ice; or (2) failure induced by to hydrostatic overpressure due to water accumulation. We exclude here the possibility of a critical geometry being reached, given the evidence of extreme thickness loss in recent years: first, the HG has not accumulated snow to cause an ice avalanche release as applies to "ramp" bedrock configuration HGs, and second, the PdM has a "terrace" configuration (Pralong & Funk, 2006). In scenario (1), the presence of a temperate zone—representing a transitional state between cold and temperate regimes on an otherwise cold-based glacier—is caused by the accumulation and storage of infiltrated water (Faillettaz et al., 2015). This may propagate temperate conditions to the base, reducing ice–bedrock adhesion and potentially triggering failure. In this scenario, detectable precursors prior to break-off (crevasse formation and velocity increase) would appear only a few days before failure (Faillettaz et al., 2011). A comparable event occurred at Altels Glacier in 1865 (3629 m a.s.l., Bernese Oberland, Swiss Alps). The glacier was likely entirely cold-based prior to rapid warming and a transition to temperate conditions in its lower part, promoting the accumulation of liquid water at the glacier bed and ultimately leading to catastrophic collapse (Faillettaz et al., 2011, 2016). At PdM, the possibility of a temperate zone cannot be excluded without direct basal measurements in this zone. In scenario (2), the presence of sufficient water volumes in crevasses can also cause large ice avalanches through processes of hydraulic jacking and fracturing, regardless of the basal thermal condition, as occurred at Marmolada, Italian Alps (Bondesan & Francese, 2023; Francese et al., 2025). In this case, cold residual ice was left at the base, showing that the ice was cold based and the failure plane was in the first layers of ice. This means that for the PdM HG, failure cannot be excluded regardless of the unknown basal-thermal regime; cold-based conditions may not prevent catastrophic failure in any case and may even predispose it by the blocking of englacial or subglacial channels with cold ice.

https://doi.org/10.5194/egusphere-2026-2455
Preprint. Discussion started: 11 June 2026


### 5.3. Permafrost conditions and relationship with the hanging glacier

Our results show that permafrost around the PdM summit is discontinuous, occurring primarily on north facing terrain. South facing slopes are either permafrost free or frozen depending on opposing ridge conditions. This is consistent with Magnin et al. (2017), who showed with modelling that permafrost has disappeared in alpine rock walls with southerly aspects up to 3300 m a.s.l. However, it contradicts both the Alpine Permafrost Index Map (APIM) predictions of permafrost in all ground conditions at the PdM summit (Boeckli et al., 2012); and from the Permafrost and Ground Ice Map (PGIM) which predicts ground temperatures of colder than -3 °C on the N and E aspects, and -2 to -3 °C on the W aspect (Kenner et al., 2019). Such findings align with other fine-scale site investigations which frequently find that low resolution permafrost map products insufficiently account for strong topographical controls on Alpine ground thermal conditions (*i.e.* Cathala et al., 2024; Haberkorn et al., 2015; Magnin et al., 2017). Summit ridges at PdM are relatively thin (PM_E3–PM_SW1 = 40 m, PM_N1–PM_E2 = 65 m), permitting strong lateral heat flux gradients (Noetzli et al., 2007). On the NW–SE summit ridge, both faces are warmed by solar irradiation; thermal modelling indicates that this precludes the presence of permafrost in the upper ridge (Fig. 11). This is consistent with the ERT data, which show a 20–25 m thick unfrozen internal layer, and permafrost only occurring where ridge thickness exceeds ~90 m. (Fig. 12a). Modelling further suggests that the upper ridge is too thin to have sustained permafrost since ~1954. This exceeds the observations of Haberkorn et al. (2015), who demonstrated that permafrost persists within a 40 m wide alpine ridge at 2900 m a.s.l.; however, in that case thermal forcing was strongly asymmetric, as the ridge was bordered by north- and south-facing rock walls. Similar topographical configuration at PdM partly explains the persistence of permafrost at PM_E2, with negative heat flux from the north facing side of the SW–NE ridge (PM_N1 MARST = –3.7 °C).

At ERT-2, unfrozen bedrock is maintained by heat flux from the south face, with permafrost only appearing in thicker sections of the ridge cross section (~130 m wide). The doubling of ALT since 2015 at PM_E2 and PM_N1 is consistent with warming trends observed in the Alps (Magnin et al., 2024; Noetzli et al., 2024; PERMOS, 2024) driven by record breaking Swiss air temperatures over the period 2014–2025 (MeteoSwiss, 2026). We hypothesise that the unfrozen cores in both ERT-1 and ERT-2 are indicative of water infiltration into the fractured rock wall, with drainage occurring along schistosity planes and interconnected joints (*i.e.* Offer et al., 2025; Fig. 12). As the piezometric level has been shown to lie several hundred metres below the summit of the Aiguille du Midi (3842 m a.s.l., Mont-Blanc massif, France) (Magnin & Josnin, 2021), saturated conditions are only possible if fractures are sealed by ice, preventing drainage. However, several factors complicate the ERT interpretation. Anisotropy related to the gneissic lithology may influence electrical current pathways, potentially obscuring or mimicking fracture-related signals. In isolated summit settings such as PdM, fractures may drain and become air-filled, producing resistivity values similar to the surrounding bedrock. More frequent ERT monitoring would therefore be required to better resolve these hydrothermal processes, as water within fractures may alternately drain or refreeze over time and would be more readily discernible in a time series of measurements.

https://doi.org/10.5194/egusphere-2026-2455
Preprint. Discussion started: 11 June 2026


The disproportionate increase of MARST relative to MAAT (Fig. S10) has been reported by other authors at European permafrost sites and attributed to changing snow cover (Etzelmüller et al., 2020; Magnin et al., 2024). Ground surface temperatures in the Swiss Alps, which are strongly influenced by snow cover, increased by 0.4–0.6 °C over 25 years (PERMOS, 2024). Our thermal modelling indicates significant warming at 10 m depth in permafrost at PM_N1 and PM_E2 of +0.68 °C between 2000 and 2024 (Fig. S12), broadly consistent with borehole measurements from other Alpine studies (Etzelmüller et al., 2020; Haberkorn et al., 2021; Magnin et al., 2024; Noetzli et al., 2024). This increase in MARST has led to a doubling of ALT at PM_N1 and PM_E2 since 2015, indicating clear permafrost degradation at the site. Despite this warming, MARST at PM_N1 (-3.7 °C) indicates persistent permafrost conditions on the north-facing slopes surrounding the HG, and likely also beneath the HG itself. Permafrost is confirmed beneath the HG at borehole B1 (-3.0 °C; altitude 3516 m a.s.l.). At borehole B2 (3388 m a.s.l.), basal temperature was not measured, and permafrost conditions could therefore not be confirmed. However, the proximity of B2 to PM_N1 (3427 m a.s.l.), together with the continued presence of ice − even if partly or fully temperate − strongly suggests that permafrost is also present beneath the lower HG. Our data do not allow us to isolate the effects of warming in the surrounding bedrock on ice temperature, due to the interaction with the processes discussed in Sect. 5.2. Consequently, the influence of increasing MARST on permafrost beneath the HG could not be quantified.

### 5.4. Methodological limitations

Working on this HG posed significant methodological challenges. Mountaineering techniques were required to manoeuvre the GPR across the HG, making data acquisition physically demanding and slow, with teams of 3–6 people. Consequently, the dataset is sparse—two down-slope and four cross-slope profiles—limiting interpretive confidence and highlighting the value of additional survey lines. Radargrams do not always capture bedrock perpendicular to the HG surface, and reflections may also represent crevasses or other interfaces. The use of additional survey lines to create 3D bedrock profiles would improve confidence, as shown in valley glacier studies in more accessible terrain (*e.g.* Egli et al., 2021; Ruols et al., 2023). We have presented the GPR results as our best interpretation of bedrock and glacier structure. A discrepancy arose between GPR-derived ice thickness and borehole B1. Drilled to bedrock at 12.3 m on 29.07.2021, B1 is in a zone which should have been 16.9 m thick according to our UAV/GPR survey combination from 01.10.2021 and 22.09.2022. This is complicated by an unknown amount of both ice ablation/snow accumulation between the borehole installation date and UAV survey date. By September 2022, melt reduced thickness at B1 to ~9.3 m according to our DEM analysis, while the GPR survey indicates a thickness 14.6 m – a 5.3 m difference. This discrepancy exceeds the estimated error envelope of ± 3 m, which included radar resolution, bedrock picking error, and DEM resolution (± 0.05 m), though it did not include deviations from the assumed GPR wave speed (0.168 m $ns^{-1}$). Rugged subglacial topography may have produced locally thinner ice at borehole drill location. The other possibility is that the borehole did not reach bedrock when drilled. Verification would require an additional borehole, which could not be undertaken.

https://doi.org/10.5194/egusphere-2026-2455
Preprint. Discussion started: 11 June 2026


Ground temperatures exhibit high degrees of variability in mountainous terrain (Gubler et al., 2011; Haberkorn et al., 2015). As such, the CryoGrid2 results at PM_E2 and PM_N1 should be treated with caution. The model results indicate relatively warm permafrost condition at PM_E2 (MARST = 1.29 °C), even though the site lies close to the much colder north face (MARST, PM_N1 = -3.67 °C). Since PM_E2 and PM_N1 retain some snow cover (Fig. S11), this could have substantially reduce winter cooling and bias MARST upward (Haberkorn et al., 2017; Magnin et al., 2017). Because CryoGrid2 was applied in a snow-free configuration, permafrost at these locations may be colder than modelled. Furthermore, measurement points are sparse (modelling at 4 sensors) and are based on a relatively simple heat diffusion model forced by the measured RST only, which does not consider other factors such as changing snow cover over decadal periods. The only way to confirm permafrost conditions and validate our model results would be to directly measure the bedrock temperature in boreholes. This illustrates the inherent challenges of interpreting sparse datasets in environments with strong spatial heterogeneity.

### 5.5. Future of the PdM hanging glacier and others

If the high ablation rates of 2021 – 2024 persist, the HG will disappear: whether the lower HG will fail abruptly or will waste gradually remains uncertain. The HG was almost certainly cold based everywhere in the past, allowing it to form on the steep bedrock (i.e. Faillettaz et al., 2011) (PdM HG mean slope = 43 °). If the HG has transitioned to a polythermal regime at lower elevations (the HG spans 3560–3220 m a.s.l.), the temperate portion may be susceptible to catastrophic failure. Consideration should, however, be given to the long-term evolution of the HG from earlier conditions, when the glacier was substantially thicker (postcard 1942; Fig. 2a), to its present state. Notably, this progressive thinning has not resulted in catastrophic collapse to date. The concave subglacial topography may contribute to mechanical support of the ice mass, potentially stabilising zones of temperate based ice.

Since all Alpine glaciers lost significant mass in recent years (The GlaMBIE Team et al., 2025), and were heavily impacted by the heatwaves of 2022 (Cremona et al., 2023), the PdM HG is far from an isolated case. HGs in comparable topographic and climatic settings (small, isolated HGs without upstream supply of cold ice from larger accumulation areas and situated near the ELA) are likely to have undergone similar thermal and structural evolution between 2021 and 2025. The forecasted trend is for HGs in the Alps below 4000 m a.s.l. to become temperate entirely before the end of the century, with some already partially temperate (Gilbert et al., 2015). Our study at PdM partially supports this, with evidence of temperate englacial ice in the lower section. In the case of a partial collapse, the cold-based upper section would persist, with no evidence yet of the transition to temperate ice currently detectable. Cold basal conditions in the upper part of the HG are being maintained despite intense surface melting, owing to the persistently cold MAAT (–4.6 °C) and increasingly efficient winter cold wave penetration (Irvine-Fynn et al., 2011). If air temperatures are sustained at 2022–2025 levels, this HG is likely to have completely melted before the upper part becomes temperate-based, contrary to the prediction of Gilbert et al., (2015). The outlook for this HG,

https://doi.org/10.5194/egusphere-2026-2455
Preprint. Discussion started: 11 June 2026


and others like it, are their highly probable disappearance, not without the risk of catastrophic failure due to water accumulation or the development of temperature zones.

## 6. Conclusion

High thinning rates show that the Pointes du Mourti HG is strongly out of equilibrium with the current climate. Between 2021 and 2024, melt removed up to 7 ± 0.12 m of ice, accounting for 20–45 % of the 2021 thickness. At the same time, we showed that permafrost on the summit ridges is discontinuous, strongly topographically controlled, and rapidly degrading, as shown by modelled warming at depth and doubling of active layer thickness since 2015. Only shaded north-facing terrain maintains negative MARST (-3.67 °C), whereas south-facing slopes reach +3.05 °C. These results indicate a glacier-permafrost system undergoing rapid geometric and thermal adjustment to current climatic forcing.

HGs below 4000 m a.s.l. are expected to transition from cold- to polythermal-based regimes during the coming decades, with most likely to disappear. The upper ice at PdM remains cold-based, with basal temperatures below freezing (-2.77 to -2.96 °C) and currently cooling at -0.08 °C $yr^{-1}$. Despite unfavourable climatic conditions for glaciers, we show that ice thinning can partially reinforce cold-based conditions on Alpine HGs. However, vertical crevasses, exposed on the surface during the extreme summer of 2022, provide increasingly efficient drainage pathways for meltwater to penetrate the ice, potentially reaching the bedrock. This enhanced drainage results in closer alignment of the onset of spring snowmelt and basal temperature minima dates, with both minima and maxima advancing by ~2 months due to the combined effects of water infiltration and ice thinning. Consistent with this behaviour, englacial ice temperatures in the lower part of the HG − where basal temperature was not directly measured − rapidly reach temperate conditions during spring snowmelt. Here, meltwater infiltration triggers abrupt warming to 0 °C within hours, which remain stable into winter (146–193 days duration), indicating prolonged water storage in englacial and/or subglacial cavities.

The polythermal conditions we observed at PdM have important implications for stability. Meltwater-driven warming and storage may promote the development of weakly adhering temperate zones at the bed or generate hydrostatic overpressure within crevasses, both of which can trigger catastrophic failure even in otherwise cold-based glaciers, as observed in recent Alpine glacier collapses. The instability risk associated with loss of basal adhesion in the lower HG therefore cannot be excluded if temperate conditions extend to the glacier base. Small, isolated HGs near the ELA across the Alps are likely undergoing similar thermal and geometric evolution. The PdM HG is therefore likely to be indicative of widespread HG evolution under the climate-forcing conditions observed between 2021 and 2025. Alpine HGs can be expected to undergo rapid thinning, transition to polythermal regimes, and eventually disappear, with an increasing likelihood of meltwater-driven instabilities during the final stages of their evolution.

https://doi.org/10.5194/egusphere-2026-2455
Preprint. Discussion started: 11 June 2026


## 7. Author contributions

BR performed GPR and UAV data acquisition, conducted annual data collection, processed the data, created the figures (except for ERT), and wrote the initial manuscript under the supervision of CL, LR, JI, and FM. CL and JG conceptualised an earlier version of the study with LR and FM, installed the RST sensors in 2020 and performed the ERT survey in 2021. JG and LR drilled and equipped the boreholes in 2021. JI supervised the GPR investigations, provided processing code, and assisted with data analysis. LB provided technical support for the GPR and assisted with ERT and GPR data analysis. CM and AR assisted with ERT data analysis and CM provided final visualisation. JR conducted the rock sample analysis.

## 8. Acknowledgements

We acknowledge Loïc Perez, mountain guide, for his contribution to this project and for supervising most of the fieldwork campaigns. Sebastian Vivero flew the UAV and completed the photogrammetric processing for the 2021 campaign. Many others assisted with the fieldwork campaigns, and we gratefully acknowledge their support. We also thank Marcia Phillips for comments on an earlier version of this article, which greatly improved its quality.

## 9. Supplementary Material

The supplementary material for this article can be found at: link.

## 10. References

Allroggen, N., Tronicke, J., Delock, M., & Böniger, U. (2015). Topographic migration of 2D and 3D ground-penetrating radar data considering variable velocities. *Near Surface Geophysics*, *13*(3), 253–259. https://doi.org/10.3997/1873-0604.2014037

Annan, A. P. (2001). *Ground Penetrating Radar Workshop Notes*. 197.

Bender, E., Lehning, M., & Fiddes, J. (2020). Changes in Climatology, Snow Cover, and Ground Temperatures at High Alpine Locations. *Frontiers in Earth Science*, *8*, 100. https://doi.org/10.3389/feart.2020.00100

https://doi.org/10.5194/egusphere-2026-2455
Preprint. Discussion started: 11 June 2026


Boeckli, L., Brenning, A., Gruber, S., & Noetzli, J. (2012). Permafrost distribution in the European Alps: Calculation and evaluation of an index map and summary statistics. *The Cryosphere*, *6*(4), 807–820. https://doi.org/10.5194/tc-6-807-2012

Bondesan, A., & Francese, R. G. (2023). The climate-driven disaster of the Marmolada Glacier (Italy). *Geomorphology*, *431*, 108687. https://doi.org/10.1016/j.geomorph.2023.108687

Brasington, J., Langham, J., & Rumsby, B. (2003). Methodological sensitivity of morphometric estimates of coarse fluvial sediment transport. *Geomorphology*, *53*(3), 299–316. https://doi.org/10.1016/S0169-555X(02)00320-3

Cathala, M., Bock, J., Magnin, F., Ravanel, L., Ben Asher, M., Astrade, L., Bodin, X., Chambon, G., Deline, P., Faug, T., Genuite, K., Jaillet, S., Josnin, J., Revil, A., & Richard, J. (2024). Predisposing, triggering and runout processes at a permafrost-affected rock avalanche site in the French Alps (Étache, June 2020). *Earth Surface Processes and Landforms*, esp.5881. https://doi.org/10.1002/esp.5881

Côté, J., & Konrad, J.-M. (2005). Thermal conductivity of base-course materials. *Canadian Geotechnical Journal*, *42*(1), 61–78. https://doi.org/10.1139/t04-081

Cremona, A., Huss, M., Landmann, J. M., Borner, J., & Farinotti, D. (2023). European heat waves 2022: Contribution to extreme glacier melt in Switzerland inferred from automated ablation readings. *The Cryosphere*, *17*(5), 1895–1912. https://doi.org/10.5194/tc-17-1895-2023

Dai, W., Zheng, G., Antoniazza, G., Zhao, F., Chen, K., Lu, W., & Lane, S. N. (2023). Improving UAV-SfM photogrammetry for modelling high-relief terrain: Image collection strategies and ground control quantity. *Earth Surface Processes and Landforms*, *48*(14), 2884–2899. https://doi.org/10.1002/esp.5665

Draebing, D., Haberkorn, A., Krautblatter, M., Kenner, R., & Phillips, M. (2017). Thermal and Mechanical Responses Resulting From Spatial and Temporal Snow Cover Variability in Permafrost Rock Slopes, Steintaelli, Swiss Alps. *Permafrost and Periglacial Processes*, *28*(1), 140–157. https://doi.org/10.1002/ppp.1921

Duvillard, P.-A., Jauvin, M., Lempereur, H., Ghorbani, A., Corroller, L. L., Richard, J., Revil, A., Ravanel, L., & Vaudelet, P. (2024). La chapelle du Thabor (3165 m, Hautes-Alpes), un patrimoine sensible à l'évolution du permafrost de montagne. *Géomorphologie : relief, processus, environnement*, *30*(3). https://doi.org/10.4000/132bo

https://doi.org/10.5194/egusphere-2026-2455
Preprint. Discussion started: 11 June 2026


Duvillard, P.-A., Ravanel, L., Deline, P., & Dubois, L. (2018). Paraglacial Rock Slope Adjustment Beneath a High Mountain Infrastructure—The Pilatte Hut Case Study (Écrins Mountain Range, France). *Frontiers in Earth Science*, *6*, 94. https://doi.org/10.3389/feart.2018.00094

Egli, P. E., Irving, J., & Lane, S. N. (2021). Characterization of subglacial marginal channels using 3-D analysis of high-density ground-penetrating radar data. *Journal of Glaciology*, *67*(264), 759–772. https://doi.org/10.1017/jog.2021.26

Eisen, O., Nixdorf, U., Wilhelms, F., & Miller, H. (2002). Electromagnetic wave speed in polar ice: Validation of the common-midpoint technique with high-resolution dielectric-profiling and γ-density measurements. *Annals of Glaciology*, *34*, 150–156. https://doi.org/10.3189/172756402781817509

Etzelmüller, B., Guglielmin, M., Hauck, C., Hilbich, C., Hoelzle, M., Isaksen, K., Noetzli, J., Oliva, M., & Ramos, M. (2020). Twenty years of European mountain permafrost dynamics—The PACE legacy. *Environmental Research Letters*, *15*(10), 104070. https://doi.org/10.1088/1748-9326/abae9d

Faillettaz, J., Funk, M., & Vagliasindi, M. (2016). Time forecast of a break-off event from a hanging glacier. *The Cryosphere*, *10*(3), 1191–1200. https://doi.org/10.5194/tc-10-1191-2016

Faillettaz, J., Funk, M., & Vincent, C. (2015). Avalanching glacier instabilities: Review on processes and early warning perspectives. *Reviews of Geophysics*, *53*(2), 203–224. https://doi.org/10.1002/2014RG000466

Faillettaz, J., Sornette, D., & Funk, M. (2011). Numerical modeling of a gravity-driven instability of a cold hanging glacier: Reanalysis of the 1895 break-off of Altelsgletscher, Switzerland. *Journal of Glaciology*, *57*(205), 817–831. https://doi.org/10.3189/002214311798043852

Francese, R. G., Valentino, R., Haeberli, W., Bondesan, A., Giorgi, M., Picotti, S., Pettenati, F., Sandron, D., Ramponi, G., & Valt, M. (2025). Failure of Marmolada Glacier (Dolomites, Italy) in 2022: Data-based back analysis of possible collapse mechanisms. *Natural Hazards and Earth System Sciences*, *25*(9), 3027–3053. https://doi.org/10.5194/nhess-25-3027-2025

https://doi.org/10.5194/egusphere-2026-2455
Preprint. Discussion started: 11 June 2026


Gilbert, A., & Vincent, C. (2013). Atmospheric temperature changes over the 20th century at very high elevations in the European Alps from englacial temperatures. *Geophysical Research Letters*, *40*(10), 2102–2108. https://doi.org/10.1002/grl.50401

Gilbert, A., Vincent, C., Gagliardini, O., Krug, J., & Berthier, E. (2015). Assessment of thermal change in cold avalanching glaciers in relation to climate warming: COLD AVALANCHING GLACIERS INSTABILITY. *Geophysical Research Letters*, *42*(15), 6382–6390. https://doi.org/10.1002/2015GL064838

Gilbert, A., Vincent, C., Six, D., Wagnon, P., Piard, L., & Ginot, P. (2014). Modeling near-surface firn temperature in a cold accumulation zone (Col du Dôme, French Alps): From a physical to a semi-parameterized approach. *The Cryosphere*, *8*(2), 689–703. https://doi.org/10.5194/tc-8-689-2014

Gruber, S. (2005). *Mountain permafrost: Transient spatial modelling, model verification and the use of remote sensing*. https://doi.org/10.5167/uzh-18100

Gruber, S., Hoelzle, M., & Haeberli, W. (2004). Permafrost thaw and destabilization of Alpine rock walls in the hot summer of 2003. *Geophysical Research Letters*, *31*(13). https://doi.org/10.1029/2004GL020051

Gubler, S., Fiddes, J., Keller, M., & Gruber, S. (2011). Scale-dependent measurement and analysis of ground surface temperature variability in alpine terrain. *The Cryosphere*, *5*(2), 431–443. https://doi.org/10.5194/tc-5-431-2011

Guillet, G., & Ravanel, L. (2020). Variations in surface area of six ice aprons in the Mont-Blanc massif since the Little Ice Age. *Journal of Glaciology*, *66*(259), 777–789. https://doi.org/10.1017/jog.2020.46

Haberkorn, A., Kenner, R., Noetzli, J., & Phillips, M. (2021). Changes in Ground Temperature and Dynamics in Mountain Permafrost in the Swiss Alps. *Frontiers in Earth Science*, *9*, 626686. https://doi.org/10.3389/feart.2021.626686

Haberkorn, A., Phillips, M., Kenner, R., Rhyner, H., Bavay, M., Galos, S. P., & Hoelzle, M. (2015). Thermal regime of rock and its relation to snow cover in steep alpine rock walls: Gemsstock, central swiss alps. *Geografiska Annaler: Series A, Physical Geography*, *97*(3), 579–597. https://doi.org/10.1111/geoa.12101

Haberkorn, A., Wever, N., Hoelzle, M., Phillips, M., Kenner, R., Bavay, M., & Lehning, M. (2017). Distributed snow and rock temperature modelling in steep rock walls using Alpine3D. *The Cryosphere*, *11*(1), 585–607. https://doi.org/10.5194/tc-11-585-2017

https://doi.org/10.5194/egusphere-2026-2455
Preprint. Discussion started: 11 June 2026


Haeberli, W., Noetzli, J., Arenson, L., Delaloye, R., Gärtner-Roer, I., Gruber, S., Isaksen, K., Kneisel, C., Krautblatter, M., & Phillips, M. (2010). Mountain permafrost: Development and challenges of a young research field. *Journal of Glaciology*, *56*(200), 1043–1058. https://doi.org/10.3189/002214311796406121

Harrison, C. H. (1970). Reconstruction of subglacial relief from radio echo sounding records. *Geophysics*, *35*(6), 1099–1115. https://doi.org/10.1190/1.1440146

Hartmeyer, I., Delleske, R., Keuschnig, M., Krautblatter, M., Lang, A., Schrott, L., & Otto, J.-C. (2020). Current glacier recession causes significant rockfall increase: The immediate paraglacial response of deglaciating cirque walls. *Earth Surface Dynamics*, *8*(3), 729–751. https://doi.org/10.5194/esurf-8-729-2020

Hartmeyer, I., & Otto, J.-C. (2024). Rockfall, glacier recession, and permafrost degradation: Long-term monitoring of climate change impacts at the Open-Air-Lab Kitzsteinhorn, Hohe Tauern. *DEUQUA Special Publications*, *5*, 3–12. https://doi.org/10.5194/deuquasp-5-3-2024

Hasler, A., Gruber, S., & Haeberli, W. (2011). *Temperature variability and thermal offset in steep alpine rock and ice faces* [Preprint]. Frozen Ground. https://doi.org/10.5194/tcd-5-721-2011

Hauck, C., & Hilbich, C. (2024). Preconditioning of mountain permafrost towards degradation detected by electrical resistivity. *Environmental Research Letters*, *19*(6), 064010. https://doi.org/10.1088/1748-9326/ad3c55

Herring, T., Lewkowicz, A. G., Hauck, C., Hilbich, C., Mollaret, C., Oldenborger, G. A., Uhlemann, S., Farzamian, M., Calmels, F., & Scandroglio, R. (2023). Best practices for using electrical resistivity tomography to investigate permafrost. *Permafrost and Periglacial Processes*, *34*(4), 494–512. https://doi.org/10.1002/ppp.2207

Heucke, E. (1999). A Light Portable Steam-driven Ice Drill Suitable for Drilling Holes in Ice and Firn. *Geografiska Annaler, Series A: Physical Geography*, *81*(4), 603–609. https://doi.org/10.1111/j.0435-3676.1999.00088.x

Irvine-Fynn, T. D. L., Hodson, A. J., Moorman, B. J., Vatne, G., & Hubbard, A. L. (2011). POLYTHERMAL GLACIER HYDROLOGY: A REVIEW. *Reviews of Geophysics*, *49*(4), 2010RG000350. https://doi.org/10.1029/2010RG000350

https://doi.org/10.5194/egusphere-2026-2455
Preprint. Discussion started: 11 June 2026


James, M. R., Antoniazza, G., Robson, S., & Lane, S. N. (2020). Mitigating systematic error in topographic models for geomorphic change detection: Accuracy, precision and considerations beyond off-nadir imagery. *Earth Surface Processes and Landforms*, *45*(10), 2251–2271. https://doi.org/10.1002/esp.4878

James, M. R., Robson, S., d'Oleire-Oltmanns, S., & Niethammer, U. (2017). Optimising UAV topographic surveys processed with structure-from-motion: Ground control quality, quantity and bundle adjustment. *Geomorphology*, *280*, 51–66. https://doi.org/10.1016/j.geomorph.2016.11.021

Kaushik, S., Ravanel, L., Magnin, F., Yan, Y., Trouve, E., & Cusicanqui, D. (2021). DISTRIBUTION AND EVOLUTION OF ICE APRONS IN A CHANGING CLIMATE IN THE MONT-BLANC MASSIF (WESTERN EUROPEAN ALPS). *The International Archives of the Photogrammetry, Remote Sensing and Spatial Information Sciences*, *XLIII-B3-2021*, 469–475. https://doi.org/10.5194/isprs-archives-XLIII-B3-2021-469-2021

Kenner, R., Noetzli, J., Hoelzle, M., Raetzo, H., & Phillips, M. (2019). Distinguishing ice-rich and ice-poor permafrost to map ground temperatures and ground ice occurrence in the Swiss Alps. *The Cryosphere*, *13*(7), 1925–1941. https://doi.org/10.5194/tc-13-1925-2019

Krautblatter, M., & Hauck, C. (2007). Electrical resistivity tomography monitoring of permafrost in solid rock walls. *Journal of Geophysical Research: Earth Surface*, *112*(F2), 2006JF000546. https://doi.org/10.1029/2006JF000546

Kyriou, A., Nikolakopoulos, K., & Koukouvelas, I. (2021). How Image Acquisition Geometry of UAV Campaigns Affects the Derived Products and Their Accuracy in Areas with Complex Geomorphology. *ISPRS International Journal of Geo-Information*, *10*(6), 408. https://doi.org/10.3390/ijgi10060408

Lambiel, C., Maillard, B., Kummert, M., & Reynard, E. (2016). Geomorphology of the Hérens valley (Swiss Alps). *Journal of Maps*, *12*(1), 160–172. https://doi.org/10.1080/17445647.2014.999135

Lane, S. N., Westaway, R. M., & Murray Hicks, D. (2003). Estimation of erosion and deposition volumes in a large, gravel-bed, braided river using synoptic remote sensing. *Earth Surface Processes and Landforms*, *28*(3), 249–271. https://doi.org/10.1002/esp.483

https://doi.org/10.5194/egusphere-2026-2455
Preprint. Discussion started: 11 June 2026


Magnin, F., Deline, P., Ravanel, L., Noetzli, J., & Pogliotti, P. (2015). Thermal characteristics of permafrost in the steep alpine rock walls of the Aiguille du Midi (Mont Blanc Massif, 3842 m a.s.l). *The Cryosphere*, *9*(1), 109–121. https://doi.org/10.5194/tc-9-109-2015

Magnin, F., & Josnin, J.-Y. (2021). Water Flows in Rock Wall Permafrost: A Numerical Approach Coupling Hydrological and Thermal Processes. *Journal of Geophysical Research: Earth Surface*, *126*(11), e2021JF006394. https://doi.org/10.1029/2021JF006394

Magnin, F., Josnin, J.-Y., Ravanel, L., Pergaud, J., Pohl, B., & Deline, P. (2017). Modelling rock wall permafrost degradation in the Mont Blanc massif from the LIA to the end of the 21st century. *The Cryosphere*, *11*(4), 1813–1834. https://doi.org/10.5194/tc-11-1813-2017

Magnin, F., Ravanel, L., Bodin, X., Deline, P., Malet, E., Krysiecki, J., & Schoeneich, P. (2024). Main results of permafrost monitoring in the French Alps through the *PermaFrance* network over the period 2010–2022. *Permafrost and Periglacial Processes*, *35*(1), 3–23. https://doi.org/10.1002/ppp.2209

MeteoSwiss. (2025). *MétéoSuisse 2025: Bulletin climatologique année 2024. Genève.*

MeteoSwiss. (2026). *MétéoSuisse 2026: Bulletin climatologique année 2025. Genève.*

Mollaret, C., Hilbich, C., Pellet, C., Flores-Orozco, A., Delaloye, R., & Hauck, C. (2019). Mountain permafrost degradation documented through a network of permanent electrical resistivity tomography sites. *The Cryosphere*, *13*(10), 2557–2578. https://doi.org/10.5194/tc-13-2557-2019

Mouginot, J., Rignot, E., Gim, Y., Kirchner, D., & Le Meur, E. (2014). Low-frequency radar sounding of ice in East Antarctica and southern Greenland. *Annals of Glaciology*, *55*. https://doi.org/10.3189/2014AoG67A089

Murray, T., Stuart, G. W., Fry, M., Gamble, N. H., & Crabtree, M. D. (2000). Englacial water distribution in a temperate glacier from surface and borehole radar velocity analysis. *Journal of Glaciology*, *46*(154), 389–398. https://doi.org/10.3189/172756500781833188

Noetzli, J., Gruber, S., Kohl, T., Salzmann, N., & Haeberli, W. (2007). Three-dimensional distribution and evolution of permafrost temperatures in idealized high-mountain topography. *Journal of Geophysical Research: Earth Surface*, *112*(F2). https://doi.org/10.1029/2006JF000545

https://doi.org/10.5194/egusphere-2026-2455
Preprint. Discussion started: 11 June 2026


Noetzli, J., Isaksen, K., Barnett, J., Christiansen, H. H., Delaloye, R., Etzelmüller, B., Farinotti, D., Gallemann, T., Guglielmin, M., Hauck, C., Hilbich, C., Hoelzle, M., Lambiel, C., Magnin, F., Oliva, M., Paro, L., Pogliotti, P., Riedl, C., Schoeneich, P., … Phillips, M. (2024). Enhanced warming of European mountain permafrost in the early 21st century. *Nature Communications*, *15*(1), 10508. https://doi.org/10.1038/s41467-024-54831-9

Offer, M., Weber, S., Krautblatter, M., Hartmeyer, I., & Keuschnig, M. (2025). Pressurised water flow in fractured permafrost rocks revealed by borehole temperature, electrical resistivity tomography, and piezometric pressure. *The Cryosphere*, *19*(1), 485–506. https://doi.org/10.5194/tc-19-485-2025

PERMOS. (2024). *PERMOS Bulletin 2023*. PERMOS 2024. Swiss Permafrost Bulletin 2023. Noetzli, J. and Pellet, C. (eds.). No. 5, 25 pp., doi: 10.13093/permos-bull-24.

Pralong, A., & Funk, M. (2006). On the instability of avalanching glaciers. *Journal of Glaciology*, *52*(176), 31–48. https://doi.org/10.3189/172756506781828980

Ravanel, L., Guillet, G., Kaushik, S., Preunkert, S., Malet, E., Magnin, F., Trouvé, E., Montagnat, M., Yan, Y., & Deline, P. (2023). Ice aprons on steep high-alpine slopes: Insights from the Mont-Blanc massif, Western Alps. *Journal of Glaciology*, 1–17. https://doi.org/10.1017/jog.2023.15

Rico, I., Magnin, F., López Moreno, J. I., Serrano, E., Alonso-González, E., Revuelto, J., Hughes-Allen, L., & Gómez-Lende, M. (2021). First evidence of rock wall permafrost in the Pyrenees (Vignemale peak, 3,298 m a.s.l., 42°46′16″N/0°08′33″W). *Permafrost and Periglacial Processes*, *32*(4), 673–680. https://doi.org/10.1002/ppp.2130

Roncoroni, M., Mancini, D., Kohler, T. J., Miesen, F., Gianini, M., Battin, T. J., & N. Lane, S. (2022). Centimeter-scale mapping of phototrophic biofilms in glacial forefields using visible band ratios and UAV imagery. *International Journal of Remote Sensing*, *43*(13), 4723–4757. https://doi.org/10.1080/01431161.2022.2079963

Rücker, C., Günther, T., & Wagner, F. M. (2017). pyGIMLi: An open-source library for modelling and inversion in geophysics. *Computers & Geosciences*, *109*, 106–123. https://doi.org/10.1016/j.cageo.2017.07.011

Ruols, B., Baron, L., & Irving, J. (2023). Development of a drone-based ground-penetrating radar system for efficient and safe 3D and 4D surveying of alpine glaciers. *Journal of Glaciology*, 1–12. https://doi.org/10.1017/jog.2023.83

https://doi.org/10.5194/egusphere-2026-2455
Preprint. Discussion started: 11 June 2026


Schroeder, D. M., Bingham, R. G., Blankenship, D. D., Christianson, K., Eisen, O., Flowers, G. E., Karlsson, N. B., Koutnik, M. R., Paden, J. D., & Siegert, M. J. (2020). Five decades of radioglaciology. *Annals of Glaciology*, *61*(81), 1–13. https://doi.org/10.1017/aog.2020.11

SCNAT. (2022, September 28). *Worse than 2003: Swiss glaciers are melting more than ever before*. Swiss Commission for Cryosphere Observation (SCC), Swiss Academy of Sciences (SCNAT). https://scnat.ch/en/id/qPn2w

SCNAT. (2024, October 1). *Severe melting of glaciers despite heavy snowfall at high altitudes*. Swiss Commission for Cryosphere Observation (SCC), Swiss Academy of Sciences (SCNAT). https://scnat.ch/…/Severe_melting_of_glaciers_despite_heavy_snowfall_at_high_altitudes

Stott, E., Williams, R. D., & Hoey, T. B. (2020). Ground Control Point Distribution for Accurate Kilometre-Scale Topographic Mapping Using an RTK-GNSS Unmanned Aerial Vehicle and SfM Photogrammetry. *Drones*, *4*(3), Article 3. https://doi.org/10.3390/drones4030055

The GlaMBIE Team, Zemp, M., Jakob, L., Dussaillant, I., Nussbaumer, S. U., Gourmelen, N., Dubber, S., A, G., Abdullahi, S., Andreassen, L. M., Berthier, E., Bhattacharya, A., Blazquez, A., Boehm Vock, L. F., Bolch, T., Box, J., Braun, M. H., Brun, F., Cicero, E., … Zheng, W. (2025). Community estimate of global glacier mass changes from 2000 to 2023. *Nature*, *639*(8054), 382–388. https://doi.org/10.1038/s41586-024-08545-z

Vivero, S., Hendrickx, H., Frankl, A., Delaloye, R., & Lambiel, C. (2022). Kinematics and geomorphological changes of a destabilising rock glacier captured from close-range sensing techniques (Tsarmine rock glacier, Western Swiss Alps). *Frontiers in Earth Science*, *10*, 1017949. https://doi.org/10.3389/feart.2022.1017949

Vivero, S., & Lambiel, C. (2019). Monitoring the crisis of a rock glacier with repeated UAV surveys. *Geographica Helvetica*, *74*(1), 59–69. https://doi.org/10.5194/gh-74-59-2019

Weber, S., Beutel, J., Da Forno, R., Geiger, A., Gruber, S., Gsell, T., Hasler, A., Keller, M., Lim, R., Limpach, P., Meyer, M., Talzi, I., Thiele, L., Tschudin, C., Vieli, A., Vonder Mühll, D., & Yücel, M. (2019). A decade of detailed observations (2008–2018) in steep bedrock permafrost at the Matterhorn Hörnligrat (Zermatt, CH). *Earth System Science Data*, *11*(3), 1203–1237. https://doi.org/10.5194/essd-11-1203-2019

https://doi.org/10.5194/egusphere-2026-2455
Preprint. Discussion started: 11 June 2026


Westermann, S., Schuler, T. V., Gisnås, K., & Etzelmüller, B. (2013). Transient thermal modeling of permafrost conditions in Southern Norway. *The Cryosphere*, *7*(2), 719–739. https://doi.org/10.5194/tc-7-719-2013

Žabota, B., & Kobal, M. (2021). Accuracy Assessment of UAV-Photogrammetric-Derived Products Using PPK and GCPs in Challenging Terrains: In Search of Optimized Rockfall Mapping. *Remote Sensing*, *13*(19), 3812. https://doi.org/10.3390/rs13193812

Zimmermann, E., Kemna, A., Berwix, J., Glaas, W., Münch, H. M., & Huisman, J. A. (2008). A high-accuracy impedance spectrometer for measuring sediments with low polarizability. *Measurement Science and Technology*, *19*(10), 105603. https://doi.org/10.1088/0957-0233/19/10/105603